Draft version December 30, 2022
Typeset using LaTeX **preprint** style in AASTeX62

N-body simulations of the Self–Confinement of Viscous Self–Gravitating Narrow Eccentric Planetary Ringlets

Joseph M. Hahn,[1] Douglas P. Hamilton,[2] Thomas Rimlinger,[2] and Lucy Luu[2]

[1] *Space Science Institute*
[2] *University of Maryland*

(Received not yet; Revised not yet; Accepted not yet)

Submitted to Somewhere, eventually

ABSTRACT

N-body simulations are used to illustrate how a viscous self-gravitating narrow eccentric planetary ringlet can evolve into a self–confining state.

Keywords: editorials, notices — miscellaneous — catalogs — surveys — update, me

1. INTRODUCTION

Narrow eccentric planetary ringlets have properties both interesting and not well understood: sharp edges, sizable eccentricity gradients, and a confinement mechanism that opposes radial spreading due to ring viscosity. To date, nearly all of the prevailing ringlet confinement mechanisms assume that there also exists a pair of unseen shepherd satellites that straddle the ringlet, with those shepherds' gravities also torquing the ringlet's edges' in a way that keeps it radially confined (Goldreich & Tremaine 1979a,b, 1981; Chiang & Goldreich 2000; Mosqueira & Estrada 2002). However the Cassini spacecraft failed to detect any such shepherds near Saturn's narrow ringlets, which casts doubt upon that confinement mechanism (Longaretti 2018). Note though that Borderies et al. (1982) showed that a viscous ringlet that has a sufficiently high eccentricity gradient can in fact be self-confining, due to the resulting reversal of the viscous angular momentum flux. Which motivates this study, which uses the epi_int_lite N-body integrator to investigate whether a viscous and self–gravitating ringlet might evolve into a self-confining state.

2. EPI_INT_LITE

Epi_int_lite is a child of the epi_int N-body integrator that was used to simulate the outer edge of Saturn's B ring while it is sculpted by satellite perturbations (Hahn & Spitale 2013). The new code is very similar to its parent but differs in two significant ways: (*i.*) epi_int_lite is written in python and is recoded for more efficient execution, and (*ii.*) epi_int_lite uses a more reliable drift step to handle unperturbed motion around an oblate planet (detailed in Appendix A).

Corresponding author: Joseph M. Hahn
jhahn@spacescience.org

Otherwise epi_int_lite's treatment of ring self–gravity and viscosity are identical to that used by the parent code, see Hahn & Spitale (2013) for additional details. The epi_int_lite source code is available at https://github.com/joehahn/epi_int_lite, and the code's numerical quality is benchmarked in Appendix B where the output of several numerical experiments are compared against theoretical expectations.

Calculations by epi_int_lite use natural units with gravitation constant $G = 1$, central primary mass $M = 1$, and the ringlet's inner edge has initial radius $r_0 = 1$, and so the ringlet masses m_r and radii r quoted below are in units of M and r_0. Converting code output from natural units to physical units requires choosing physical values for M and r_0 and multiplying accordingly, and when this text does so it assumes Saturn's mass $M = 5.68 \times 10^{29}$ gm and a characteristic ring radius $r_0 = 1.0 \times 10^{10}$ cm. Simulation time t is in units of $T_{\rm orb}/2\pi$ where $T_{\rm orb} = 2\pi\sqrt{r_0^3/GM}$ is the orbit period at r_0, so divide simulation time t by 2π and multiply by $T_{\rm orb}$ to convert simulation time from natural to physical units. The simulated particles' motions during the drift step are also sensitive to the J_2 portion of the primary's non-spherical gravity component (see Appendix B), and all simulations adopt Saturn-like values of $J_2 = 0.01$ and $R_p = r_0/2$ where R_p is the planet's mean radius.

2.1. *streamlines*

Initially all particles are assigned to various streamlines across the simulated ringlet. A streamline is a closed eccentric path around the primary, and each streamline is populated by N_p particles that are initially assigned a common semimajor axis a and eccentricity e while distributed uniformly in longitude. Most of the simulations described below employ only $N_s = 2$ streamlines, so that the model output can be compared against theoretical treatments that also treat the ringlet as two gravitating streamlines (e.g. Borderies et al. 1983). But the following also performs a few higher-resolution simulations using $N_s = 5 - 31$ streamlines, to demonstrate that the $N_s = 2$ treatment is perfectly adequate and reproduces all the relevant dynamics. All simulations use $N_p = 241$ particles per streamline, and the total number of particles is $N_s N_p$. Note that the assignment of particles to a given streamline is merely for labeling purposes, as particles are still free to wander in response to the ring's internal forces, namely, ring gravity and viscosity. But as Hahn & Spitale (2013) as well as this work shows, the simulated ring stays coherent and highly organized throughout the simulation such that particles on the same streamline do not pass each other longitudinally, nor do they cross adjacent streamlines. Because the simulated ringlet stays highly organized, there is no radial or longitudinal mixing of the ring particles, and simulated particles preserve their streamline membership over time.

The epi_int_lite code also monitors all particles and checks whether any have crossed adjacent streamlines. If that happens the simulation is then terminated since the particles' subsequent evolution would no longer be computed reliably.

2.2. *N-body method*

The epi_int_lite N-body integrator uses the same drift-kick scheme used by the MERCURY Nbody algorithm (Chambers 1999) except that epi_int_lite particles that do not interact with each other directly. Rather, epi_int_lite particles are only perturbed by the accelerations exerted by the ringlet's individual streamlines. Those accelerations are sensitive to the streamline's relative separations and orientations, which are inferred from the particles' positions and velocities. Epi_int_lite particles are thus tracer particles that indicate the streamlines' locations and orientations, which the N-body integrator uses to compute the orbital evolution of those tracer particles due to the perturbations exerted by those streamlines. This streamline approach is widely used in theoretical studies of planetary rings (c.f. Goldreich & Tremaine 1979a; Borderies et al. 1983, 1985) as well as in N-body studies of rings (Hahn & Spitale 2013; Rimlinger et al. 2016). The great benefit of the streamline concept in numerical work is that it allows one to swiftly track the global evolution of the ringlet's streamlines numerically using only a modest numbers of trace particles, typically $N_s N_p \sim 500$.

The simulations reported on here account for streamline gravity and ringlet viscosity. Because a ringlet is narrow, all particles are in close proximity to the nearby portions of all streamlines, which allows us to approximate a streamline as an infinitely long wire of matter having linear density λ. Consequently the gravity of each perturbing streamline draws a particle towards that streamline with acceleration

$$A_g = \frac{2G\lambda}{\Delta}, \tag{1}$$

where Δ is the particle's distance from the streamline.

The hydrodynamic approximation is used here to account for the dissipation that occurs as particles in adjacent particle streamlines shear past and collide with the perturbed particle, without having to monitor individual particle-particle collisions. The particle's acceleration due to the ring particles' shear viscosity is

$$A_{\nu,\parallel} = -\frac{1}{\sigma r}\frac{\partial \mathcal{F}_L}{\partial r}, \tag{2}$$

where r is the particle's radial coordinate, σ is the surface density of ringlet matter, and $\mathcal{F}_{L,\nu}$ is the flux of angular momentum that is transported radially across the particle's streamline due to its collisions with particles in adjacent streamlines, *i.e.*

$$\mathcal{F}_{L,\nu} = -\nu_s \sigma r^2 \frac{\partial \omega}{\partial r} \tag{3}$$

where ν_s is the ringlet's kinematic shear viscosity and $\omega = v_\theta/r$ is the particle's angular velocity (Hahn & Spitale 2013). The acceleration $A_{\nu,\parallel}$ is parallel to the perturbed particle's streamline *i.e.* parallel to particle's velocity vector $\mathbf{v} = \dot{\mathbf{r}} = v_r\hat{r} + v_\theta\hat{\theta}$ where $\mathbf{r} = r\hat{\mathbf{r}}$ is the particle's position vector.

Dissipative collisions also transmits linear momentum in the perpendicular direction, which results in the additional acceleration

$$A_{\nu,\perp} = -\frac{1}{\sigma}\frac{\partial \mathcal{G}}{\partial r} \tag{4}$$

where the radial flux of linear momentum due to ringlet viscosity is

$$\mathcal{G} = -\left(\frac{4}{3}\nu_s + \nu_b\right)\sigma\frac{\partial v_r}{\partial r} - \left(\nu_b - \frac{2}{3}\nu_s\right)\frac{\sigma v_r}{r} \tag{5}$$

ν_b is the ringlet's kinematic bulk viscosity and v_r is the paricle's radial velocity (Hahn & Spitale 2013).

In the hydrodynamic approximation there is also the acceleration due to ringlet pressure p that is due to particle-particle collisions,

$$A_p = -\frac{1}{\sigma}\frac{\partial p}{\partial r}. \tag{6}$$

Epi_int_lite treats the particle ring as a dilute gas of colliding particles for which the 1D pressure is $p = c^2\sigma$ where c is the particles dispersion velocity. However Hahn & Spitale (2013) found ring pressure to be inconsequential in N-body simulations of Saturn's A ring, and the ringlet simulation examined in great detail in Section 3.1 also showed no sensitivity to pressure effects, so all other simulations reported on here have $c = 0$.

3. N-BODY SIMULATIONS OF VISCOUS GRAVITATING RINGLETS

The folowing describes a suite of N-body simulations of narrow viscous gravitating planetary ringlets, to highlight the range of initial ringlet conditions that do evolve into a self-confining state, and those that do not.

3.1. *nominal model*

Figure 1 shows the semimajor axis evolution of what is referred to as the nominal model since this ringlet readily evolves into a self-confining state. The simulated ringlet is composed of $N_s = 2$ streamlines having $N_p = 241$ particles per streamline, and the integrator timestep is $\Delta t = 0.5$ in natural units, so the integrator samples the particles' orbits $2\pi/\Delta t \simeq 13$ times per orbit, and this ringlet is evolved for 1.4×10^5 orbits, which requires 50 minutes execution time on a ten year old laptop. The ringlet's mass is $m_r = 10^{-10}$, its shear viscosity is $\nu_s = 10^{-13}$, and its bulk viscosity is $\nu_b = \nu_s$. The ringet's initial radial width is $\Delta a_0 = 10^{-4}$, its initial eccentricity is $e = 0.01$, and its eccentricity gradient is initially zero. A convenient measure of time is the ringlet's viscous radial spreading timescale

$$\tau_\nu = \frac{\Delta a_0^2}{12\nu_s} \tag{7}$$

which can be inferred from Eqn. (2.13) of Pringle (1981). This simulation's viscous timescale is $\tau_\nu = 8.3 \times 10^3$ in natural units or $\tau_\nu/2\pi = 1.3 \times 10^3$ orbital periods. If this ringlet were orbiting Saturn at $r_0 = 1.0 \times 10^{10}$ cm then the simulated ringlet's physical mass would be $m_r = 5.7 \times 10^{19}$ gm which is equivalent to the mass of a 24 km radius iceball assuming a volume density $\rho = 1$ gm/cm^3, and the ringlet's initial physical radial width would be $\Delta a_0 = 10^{-4} r_0 = 10$ km. This ringlet's orbit period would be $T_{orb} = 2\pi\sqrt{r_0^3/GM} = 9.0$ hours in physical units, so the ringlet's viscous timescale is $\tau_\nu = 1.4$ years, and so its shear viscosity is $\nu_s = \Delta a_0^2/12\tau_\nu = 1.9 \times 10^3$ cm^2/sec when evaluated in physical units. This ringlet's initial surface density would be $\sigma = m_r/2\pi r_0 \Delta a_0 = 900$ gm/cm^2, but Figs. 1–2 show that shrinks by a factor of about 5 as the ringlet's sememajor axis width Δa grows via viscous spreading until it settles into the self-confining state at time $t \sim 40\tau_\nu$. This so-called nominal ringlet is probably somewhat overdense and overly viscous compared to known planetary ringlets, but that is by design so that the simulated ringlet quickly settles into the self-confining state. Section 4.5 also shows how outcomes vary when a wide variety of alternate initial masses, widths, and viscosities are also considered.

Figure 3 shows that the outer streamline's eccentricity initially grows at the expense of the inner streamline's, and that is a consequence the self-gravitating ringlet's secular perturbations of itself, which is also demonstrated in Appendix C. Figure 4 shows the ringlet's eccentricity difference $\Delta e = e_{\text{outer}} - e_{\text{inner}}$ and longitude of periapse difference $\Delta\tilde{\omega} = \tilde{\omega}_{\text{outer}} - \tilde{\omega}_{\text{inner}}$, which both settle into equilibrium values after the ringlet arrives at the self-confining state.

Figure 5 shows the radii of the ringlet's two streamlines plotted versus their relative longitude $\varphi = \theta - \tilde{\omega}_{\text{inner}}$ at time $t = 100\tau_\nu$ when the simulation ends. In all simulations examined here, the ringlet's periapse twist $\Delta\tilde{\omega} = \tilde{\omega}_{\text{outer}} - \tilde{\omega}_{\text{inner}}$ is negative, so the outer streamline's longitude of periapse $\tilde{\omega}$ trails the inner streamline's, which in turn causes the streamlines' separations along the ringlet's

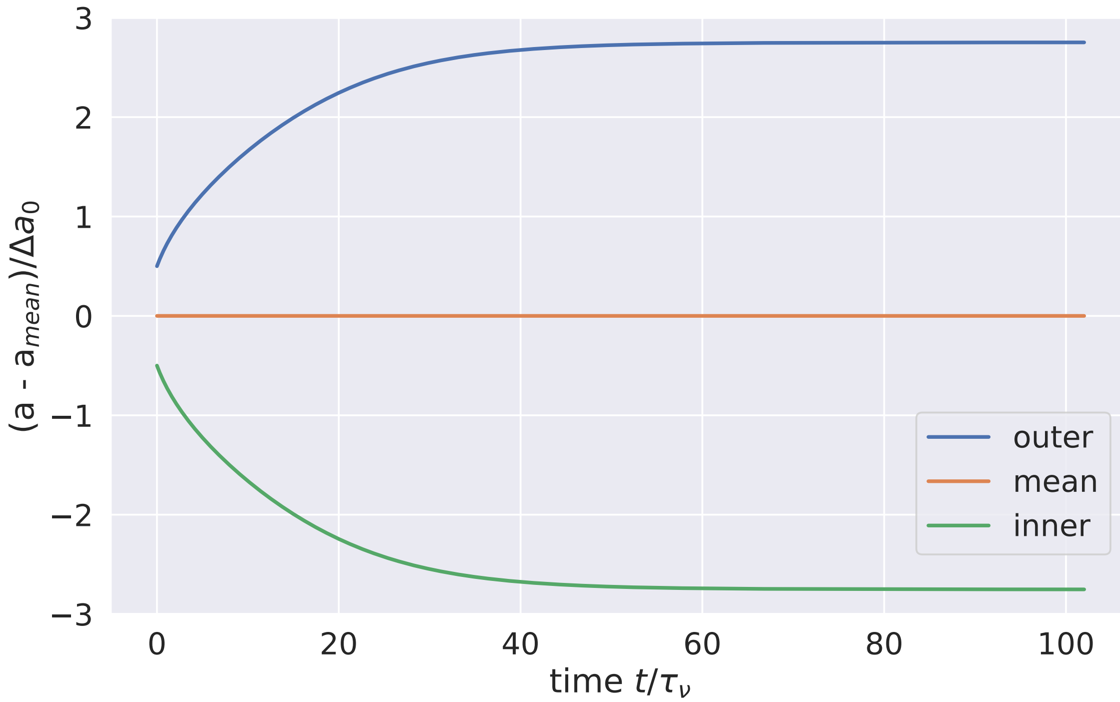

Figure 1. Evolution of the nominal ringlet's semimajor axes a versus time t in units of the ringlet's viscous timescale $\tau_\nu = 1.3 \times 10^3$ orbital periods. This ringlet is composed of $N_s = 2$ streamlines, and the outer (blue) and inner (green) streamlines' semimajor axes are plotted relative to their mean $a_{\rm mean}$, and displayed in units of the ringlet's initial width $\Delta a_0 = 10^{-4}$ in natural units (*i.e.* $G = M = r_0 = 1$). The simulated ringlet has total mass $m_r = 10^{-10}$, shear viscosity $\nu_s = 10^{-13}$, and initial eccentricity $e = 0.01$. See Section 3.1 to convert m_r, a and ν_s from natural units to physical units.

pre-periapse side (where $\varphi < 0$) to differ slightly from that int the post-periapse ($\varphi > 0$) zone. Which in turn makes the ringlet's surface density asymmetric, see Figs. 5–7.

It is convenient to recast these orbit element differences as dimensionless gradients

$$e' = a\frac{de}{da} \qquad \text{and} \qquad \tilde{\omega}' = ea\frac{d\tilde{\omega}}{da} \tag{8}$$

as these are the terms that contribute to the nonlinearity parameter of Borderies et al. (1983):

$$q = \sqrt{e'^2 + \tilde{\omega}'^2}. \tag{9}$$

See also Fig. 8 which plot's the nominal ringlet's dimensionless eccentricity gradient e', dimensionless periapse twist $\tilde{\omega}'$, and nonlinearity parameter q versus time. Most of the simulations examined here have $|\tilde{\omega}'| \ll |e'|$ so that $q \simeq |e'|$ (excepting those described in Section 4.5.1), and all simulated self-confining ringlets have a positive eccenticity gradient and a negative periapse twist such that the outer ringlet's periapse trails the inner ringlet's, consistent with the findings of Borderies et al. (1983).

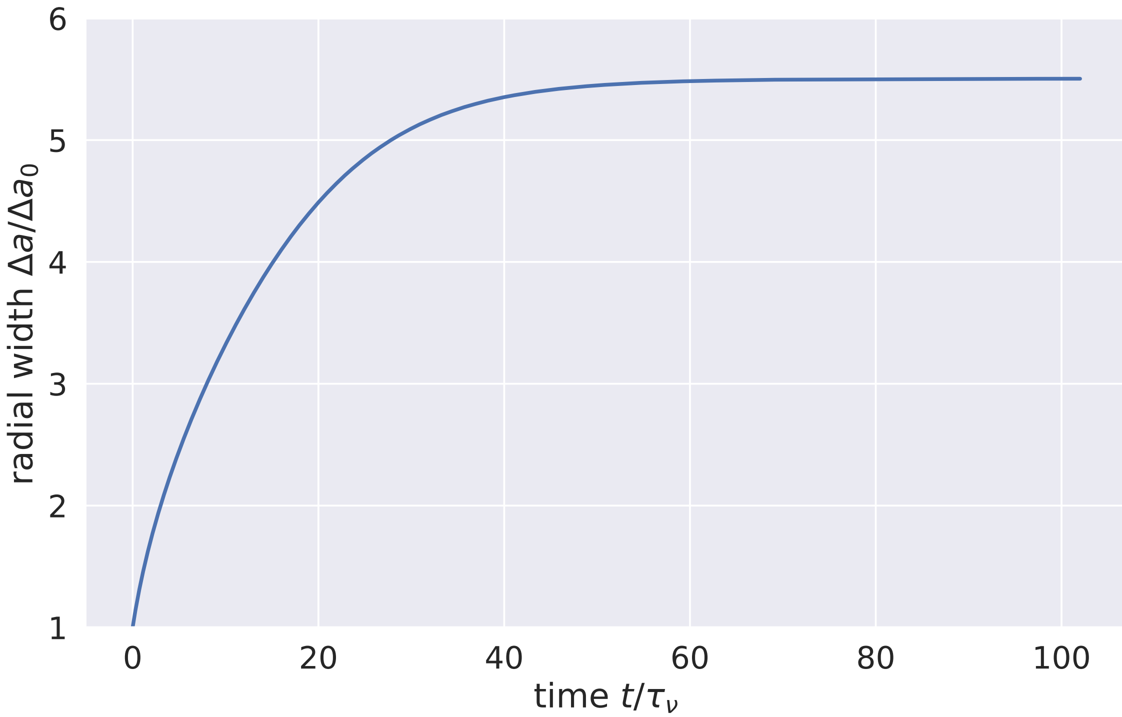

Figure 2. The nominal ringlet's semimajor axis width $\Delta a = a_{\rm outer} - a_{\rm inner}$ over time and in units of its initial radial width Δa_0.

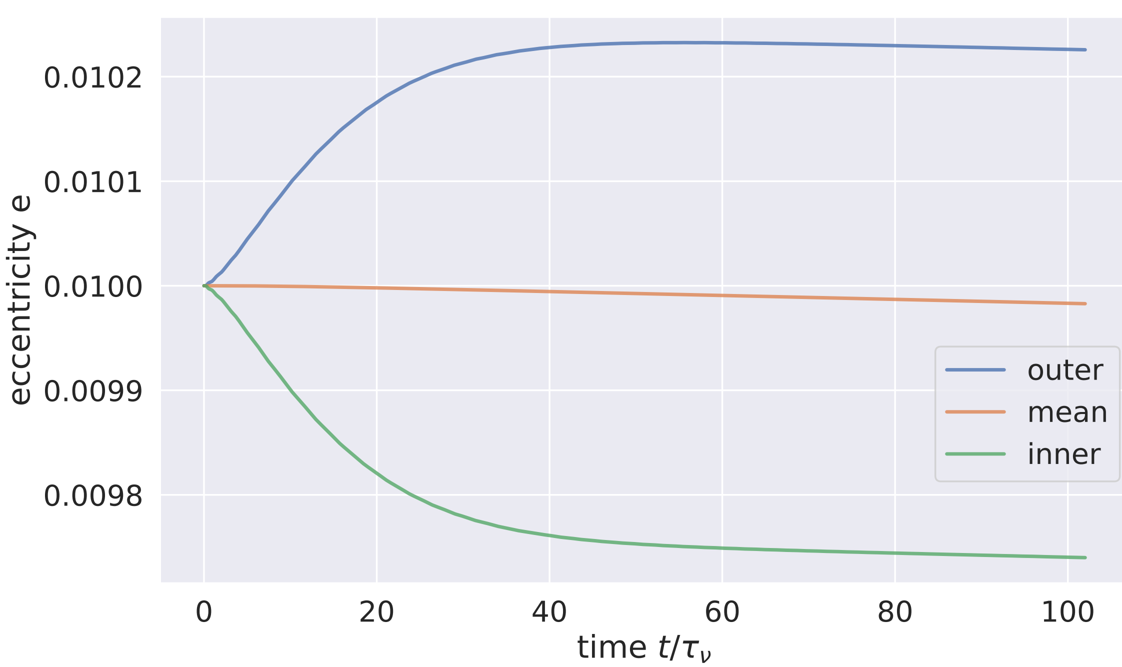

Figure 3. The nominal ringlet's eccentricity evolution.

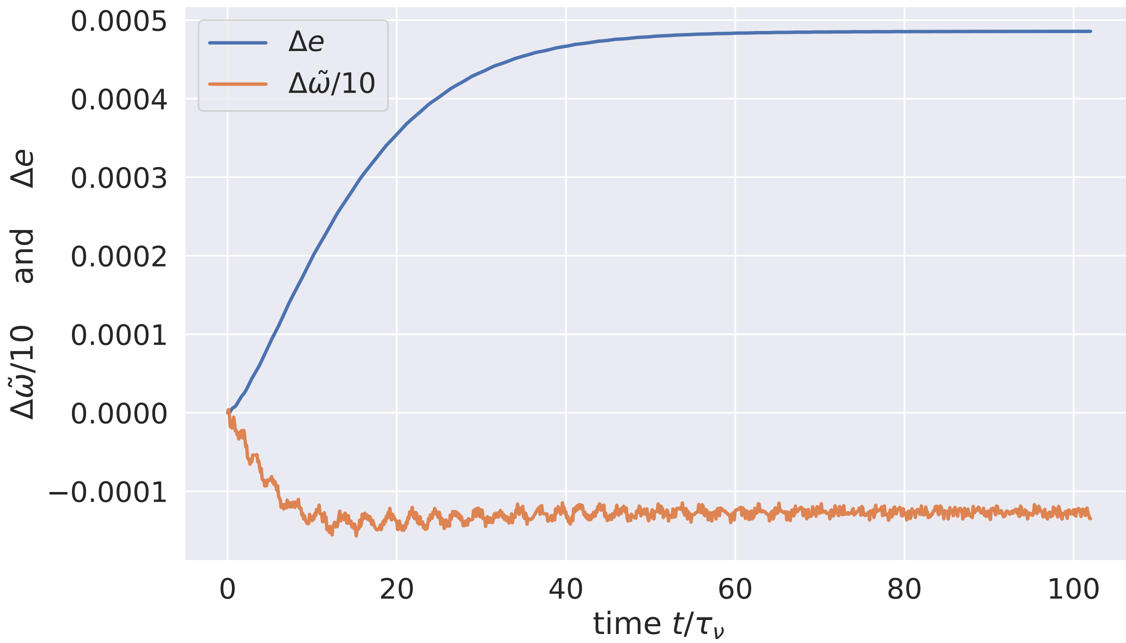

Figure 4. The nominal ringlet's eccentricity difference $\Delta e = e_{\rm outer} - e_{\rm inner}$ and longitude of periapse difference $\Delta\tilde{\omega} = \tilde{\omega}_{\rm outer} - \tilde{\omega}_{\rm inner}$ in radians divided by 10.

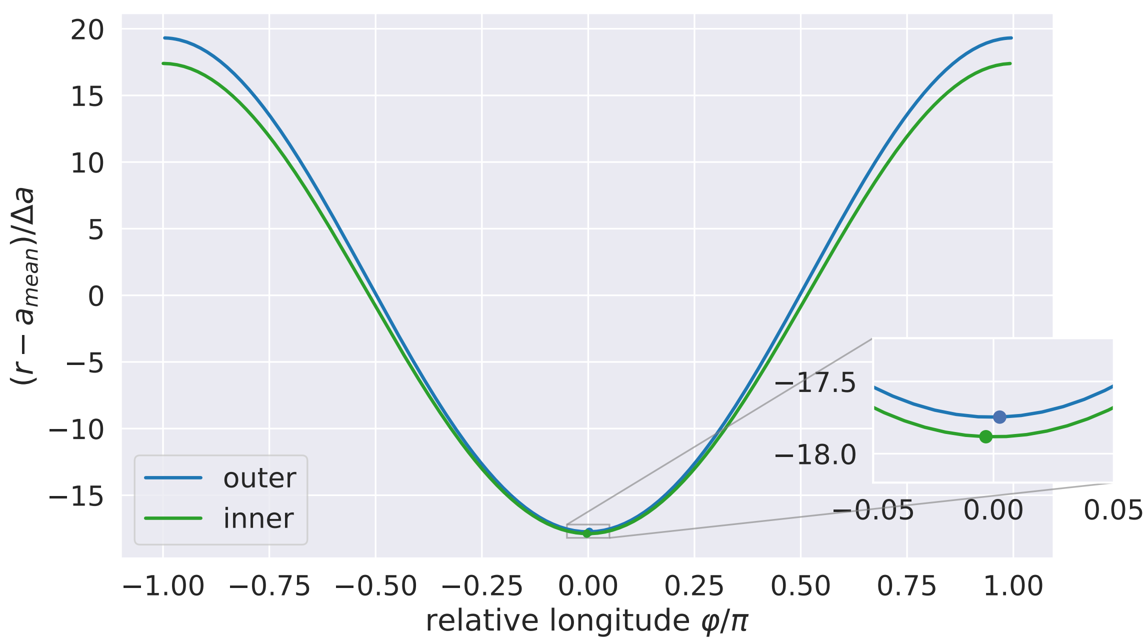

Figure 5. The radial excursions of the nominal ringlet's two streamlines are shown relative to the ringlet's mean semimajor axis a_{mean} and in units of the streamlines' semimajor axis difference Δa at time $t = 100\tau_\nu$, with that relative radial excursion being ploted versus its relative longitude $\varphi = \theta - \tilde{\omega}$. Inset plot shows that the outer streamline's longitude of periapse $\tilde{\omega}$ trailing the inner streamline's. **double-check this!!!**

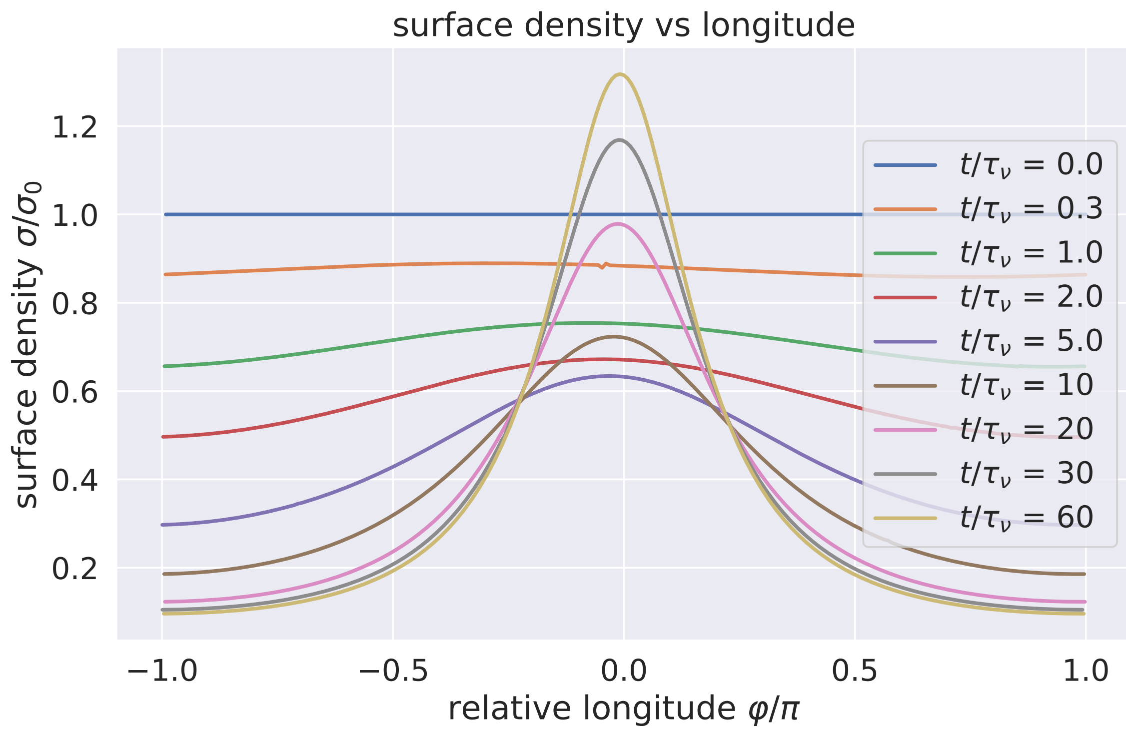

Figure 6. Nominal ringlet's surface density $\sigma(\varphi)$ versus relative longitude φ at selected times t and plotted in units of ringlet's initial mean surface density σ_0. Note that the ringlet's surface density maxima occurs just before peripase, and is due to the ringlet's negative periapse twist $\Delta\tilde{\omega} = \tilde{\omega}_{\rm outer} - \tilde{\omega}_{\rm inner} < 0$.

4. ANGULAR MOMENTUM AND ENERGY FLUXES, AND LUMINOSITIES

The nominal ringlet's evolution is readily understood when the ringlet's radial flux of angular momentum and energy are considered.

4.1. *angular momentum and energy fluxes*

The torque that is exerted on a small streamline segment of mass δm at location $\mathbf{r} = r\hat{\mathbf{r}}$ due to the streamlines orbiting interior to it is $\delta T = \delta m\mathbf{r} \times \mathbf{A}^1$ where $\mathbf{A}^1 = A_r^1\hat{\mathbf{r}} + A_\theta^1\hat{\boldsymbol{\theta}}$ is the so-called one-sided acceleration that is exerted on δm by the interior streamline. Since $\delta m = \lambda\delta\ell$ where λ is the streamline's linear mass density, and $\delta\ell$ is the segment's length, then the radial flux of angular momentum flowing into that segment due to the accelerations that are exerted by streamlines orbiting interior to that segment is

$$\mathcal{F}_L(r,\theta) = \frac{\delta T}{\delta\ell} = \lambda r A_\theta^1, \tag{10}$$

where A_θ^1 is the tangential component of the one-sided acceleration. A streamline of semimajor axis a in a ringlet having total mass m_r distributed across N_s streamlines will have a linear mass density $\lambda = m_r/N_s/2\pi a$. The radial angular momentum flux, Eqn. (10), is due to the ringlet's viscosity and self-gravity, so $\mathcal{F}_L = \mathcal{F}_{L,\nu} + \mathcal{F}_{L,g}$.

The work that the interior streamlines exert on δm as that segment travels a small distance $\delta\mathbf{r} = \mathbf{v}\delta t$ in time δt is $\delta W = \delta m\mathbf{A}^1 \cdot \delta\mathbf{r}$ where $\mathbf{v} = v_r\hat{\mathbf{r}} + v_\theta\hat{\boldsymbol{\theta}}$ is the segment's velocity, and that work accrues at δm at the rate $\delta W/\delta t = \lambda\mathbf{A}^1 \cdot \mathbf{v}\delta\ell$, so the radial flux of energy entering that ringlet segment due

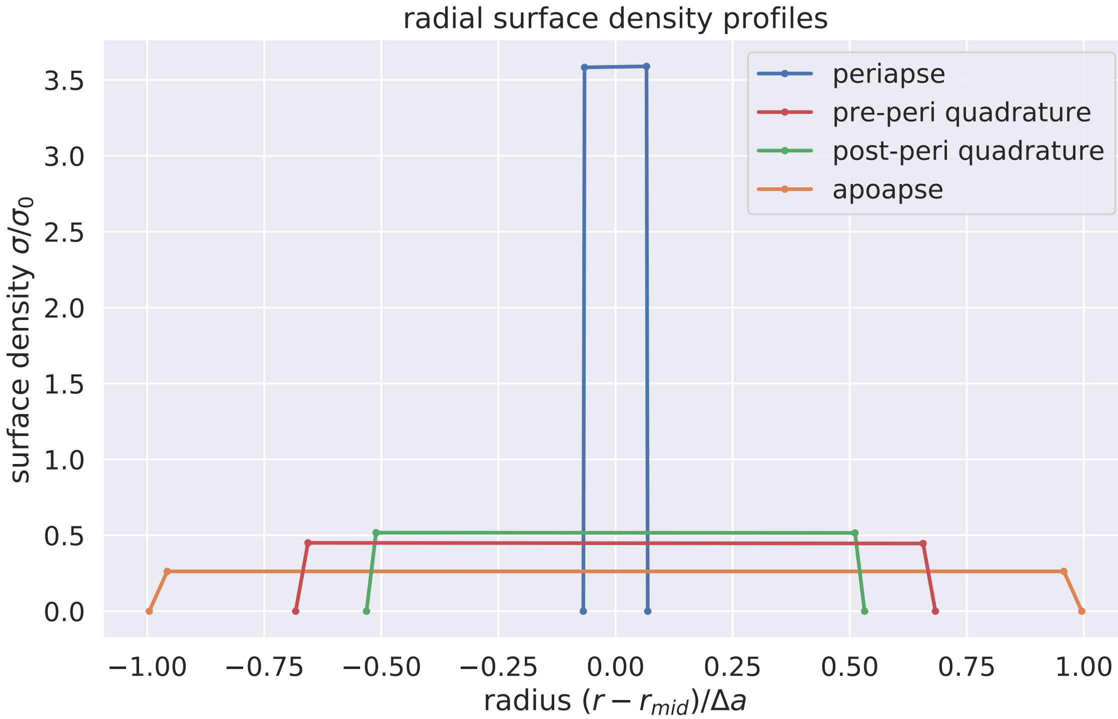

Figure 7. Radial profiles of the nominal ringlet's surface density $\sigma(\varphi)$ at time $t/\tau_\nu = 100$ when the ringlet is self-confining. Each surface density profile is plotted versus radial distance r relative to r_{mid}, which is the ringlet's midpoint along relative longitude $\varphi = \theta - \tilde{\omega}$, with those radial distances $r - r_{mid}$ measured in units of the ringlet's final semimajor axis width Δa, and surface density is shown in units of the ringlet's longitudinally-averaged surface density σ_0. Radial surface density profiles are plotted along the ringlet's periapse ($\varphi = 0$, blue curve), which is where the ringlet's streamlines are most concentrated and surface denisity σ is greatest due to the ringlet's eccentricity gradient e', at the pre-periapse quadrature ($\varphi = -\pi/2$, red curve), post-periapse quadrature ($\varphi = \pi/2$, green curve) and at apoapse ($|\varphi| = \pi$, orange curve) where streamlines have their greatest separation and ringlet surface density is lowest. This ringlet's surface density contrast between periapse and apoapse is 8.

to accelerations exerted by the interior streamlines is

$$\mathcal{F}_E(r, \theta) = \frac{\delta W}{\delta \ell \delta t} = \lambda \mathbf{A}^1 \cdot \mathbf{v}. \tag{11}$$

The radial energy flux is due to the ringlet's viscosity and self-gravity, so $\mathcal{F}_E = \mathcal{F}_{E,\nu} + \mathcal{F}_{E,g}$.

4.2. *luminosities*

The streamline containing segment δm has semimajor axis a, and integrating the radial angular momentum flux $\mathcal{F}_L$ about the entire streamline then yields the radial luminosity of angular momentum entering streamline a,

$$\mathcal{L}_L(a) = \oint \mathcal{F}_L d\ell, \tag{12}$$

which is the torque that is exerted on streamline a by those orbiting interior to it. Similarly, integrating the radial energy flux $\mathcal{F}_E$ about streamline a also yields the ringlet's radial energy luminosity

$$\mathcal{L}_E(a) = \oint \mathcal{F}_E d\ell, \tag{13}$$

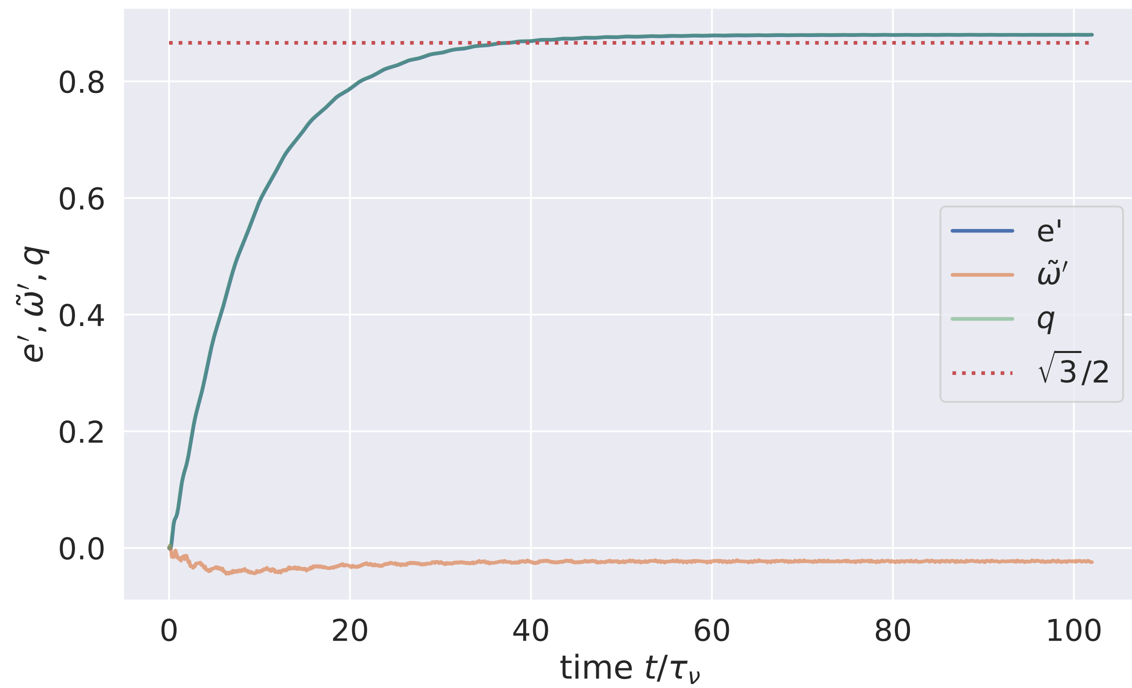

Figure 8. The nominal ringlet's dimensionless eccentricity gradient $e' = a\Delta e/\Delta a$ (blue curve), dimensionless periapse twist $\tilde{\omega}' = ea\Delta\tilde{\omega}/\Delta a$ (orange), and nonlinearity parameter $q = \sqrt{e'^2 + \tilde{\omega}'^2}$ (green curve which overlaps blue) versus time t/τ_ν. Dotted red line is the threshold for self-confinement in a non-gravitating ringlet, $e' = \sqrt{3}/2 \simeq 0.866$

which is the rate that the interior streamlines communicate energy to streamline a.

4.3. *viscous transport of angular momentum*

Angular momentum is transported radially through the ring via viscosity and self-gravity, so $\mathcal{F}_L = \mathcal{F}_{L,\nu} + \mathcal{F}_{L,g}$, where the ringlet's viscous flux of angular momentum is

$$\mathcal{F}_{L,\nu}(r,\theta) = -\nu_s \sigma r^2 \frac{\partial \omega}{\partial r} \tag{14}$$

when Eqn. (3) is written as a function of spatial coordinates and angular velocity $\omega = \dot{\theta}$. If we consider a small arc of ring material of length $d\ell$, then $\mathcal{F}_{L,\nu} d\ell$ is the torque that arc exert exerts on ring matter just exterior, due to viscous friction, so that is the rate that friction transmits angular momentum radially across that arc. And when $\mathcal{F}_{L,\nu}$ is evaluated along a single eccentric streamline of semimajor axis a, the above simplifies to

$$\mathcal{F}_{L,\nu}(a,\varphi) = \mathcal{F}_{L,\nu,c} \frac{1 - \frac{4}{3}e' \cos\varphi}{(1 - e' \cos\varphi)^2} \tag{15}$$

where $\varphi = \theta - \tilde{\omega}$ is the longitude relative to periapse and $\mathcal{F}_{L,\nu,c} = \frac{3}{2}\nu_s \sigma_0 a \Omega$ is the viscous angular momentum flux through a circular streamline of semimajor axis a and angular speed $\Omega(a)$, with Eqn. (15) assuming that $|\tilde{\omega}'| \ll e'$ so that $q \simeq e'$ (see Borderies et al. 1982 and Appendix D). Integrating the above around the streamline's circumference then yields its angular momentum luminosity,

$$\mathcal{L}_{L,\nu}(a) = \oint \mathcal{F}_{L,\nu}(a,\varphi) r d\varphi = \mathcal{L}_{L,\nu,c} \frac{1 - \frac{4}{3}e'^2}{(1 - e'^2)^{3/2}}, \tag{16}$$

which is the torque that one streamline exerts on its exterior neighbor due to viscous friction (Borderies et al. 1982 and Appendix D), with $\mathcal{L}_{L,\nu,c} = 3\pi\nu_s\sigma_0 a^2\Omega$ being the viscous angular momentum luminosity of a circular streamline.

Borderies et al. (1982) examine angular momentum transport through a viscous eccentric but non-gravitating ringlet, and use Eqns. (15–16) to show that this transport has three regimes distinguished by the ringlet's e':

1. $e' < 3/4$. The ringlet's viscous angular momentum flux $\mathcal{F}_{L,\nu}(\varphi) > 0$ at all longitudes φ. The ringlet's viscous angular momentum luminosity $\mathcal{L}_{L,\nu} > 0$, so viscous friction transports angular momentum radially outwards, and the inner ring matter evolves to smaller orbits while exterior ring matter evolves outwards, and the ringlet spreads radially.
2. $3/4 \le e' < \sqrt{3}/2$. In this regime there is a range of longitudes φ where the viscous angular momentum flux is reversed such that $\mathcal{F}_{L,\nu}(\varphi) < 0$. That angular momentum flux reversal is due to the $\partial\omega/\partial r$ term in Eqn. (3) changing sign near periapse when $e' > 0.75$, see Fig. 9. Nonetheless $\mathcal{L}_{L,\nu}$, which is proportional to the orbit-average of $\mathcal{F}_{L,\nu}(\varphi)$, is positive and the ringlet still spreads radially, albeit slower than when $e' < 0.75$.
3. $e' \ge \sqrt{3}/2$. Viscous angular momentum flux reversal is complete such that $\mathcal{L}_{L,\nu} \le 0$, viscous friction transports angular momentum radially inwards, and the ringlet shrinks radially. But if $e' = \sqrt{3}/2 \simeq 0.866$ then $\mathcal{L}_{L,\nu} = 0$ and the ringlet's radial evolution ceases, and the viscous but non-gravitating ringlet is self–confining.

Note though that the nominal ringlet's eccentricity gradient exceeds the $e' = \sqrt{3}/2 \simeq 0.866$ threshold (dotted red line in Fig. 8) when it settles into self-confinement. This is due to the ringlet's self-gravity, which also transports a flux of angular momentum $\mathcal{F}_{L,g}$ radially through the ringlet.

Figure 10 shows the nominal ringlet's viscous angular momentum flux $\mathcal{F}_{L,\nu}$ versus relative longitude $\varphi = \theta - \tilde{\omega}$ at selected times t. Early in the ringlet's evolution when time $t \le 10\tau_\nu$ (blue, orange, green, red, purple and brown curves), the ringlet is in regime 1 since $e' < 0.75$ and $\mathcal{F}_{L,\nu}(\varphi) > 0$ at all longitudes. But by time $t \ge 20\tau_\nu$ (pink curve), this ringlet's eccentricity gradient exceeds 0.75, and angular momentum flux reversal $\mathcal{F}_{L,\nu}(\varphi) < 0$ occurs near periapse where $|\varphi| \simeq 0$ where the ringlet is most overdense due to its eccentricity gradient, see also Fig. 7. This ringlet is now in regime 2 and its radial spreading is reduced by angular momentum flux reversal. And by time $t = 60\tau_\nu$ (yellow curve), this ringlet is seemingly in regime 3 since $e' > 0.866$, so one might expect the ringlet to start contracting now, but keep in mind that the above analysis ignores any transport of angular momentum via ringlet self–gravity. Figure 2 in fact shows that this gravitating ringlet's spreading had ceased by time $t \simeq 80\tau_\nu$, at which point $e' = 0.88$ (Fig. 10 yellow curve), angular momentum flux reversal is nearly complete, and the ringlet's total angular momentum luminosity $\mathcal{L}_L = \mathcal{L}_{L,\nu} + \mathcal{L}_{L,g}$ is very close to zero. Figures 11 and 12 also show that, when the ringlet is self-confining at times $t \ge 80\tau_\nu$, its small but positive viscous angular momentum luminosity $\mathcal{L}_{L,\nu} \simeq 0.006\mathcal{L}_{L,\nu,c}$ is counterbalanced by its negative gravitational angular momentum luminosity $\mathcal{L}_{L,g} \simeq -0.006\mathcal{L}_{L,\nu,c}$, at which point radial spreading has ceased and the ringlet is self-confining.

4.4. *gravitational transport*

The ringlet's viscous $\mathcal{F}_{L,\nu}$ and gravitational $\mathcal{F}_{L,g}$ angular momentum fluxes are shown Fig. 13. That figure shows how viscous friction tends to transport angular momentum radially inwards, $\mathcal{F}_{L,\nu}(\varphi) < 0$,

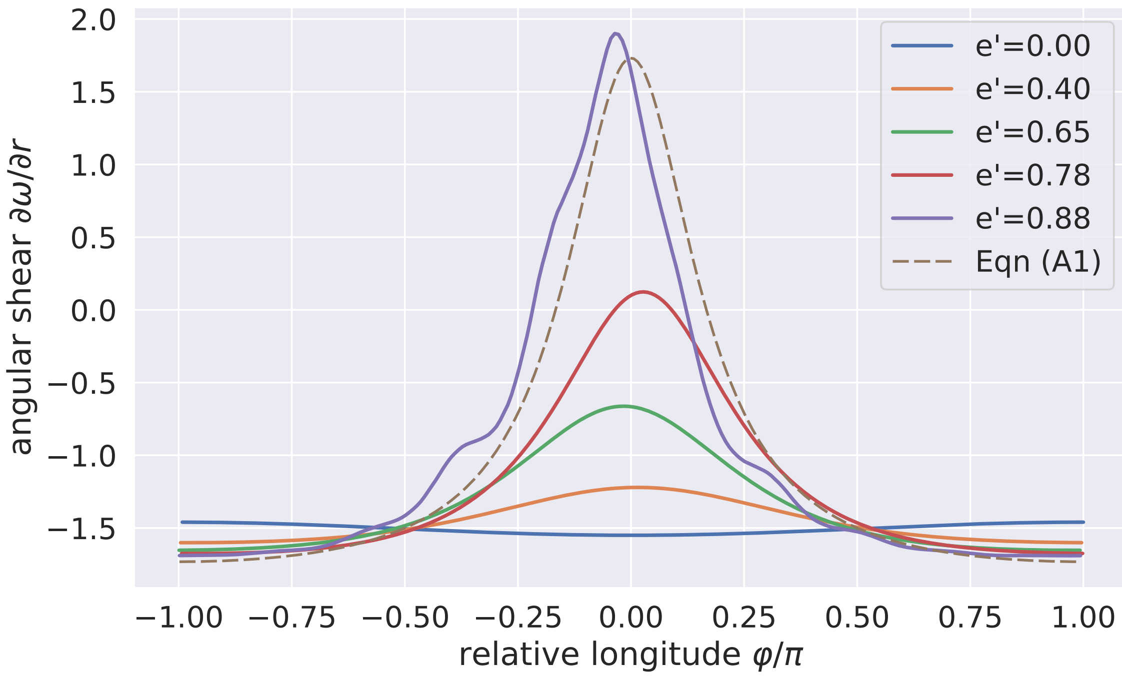

Figure 9. The nominal ringlet's angular shear $\partial\omega/\partial r$ is plotted versus relative longitude φ at selected moments in time; this quantity is negative where the inner streamline has the higher angular speed $\omega = v_\theta/r$. When the simulation starts, the ringlet has eccentricity $e = 0.01$ and eccentricity gradient $e' = 0$ so $\partial\omega/\partial r \simeq -3\Omega/2r \simeq -1.5$ when evaluated natural units (blue curve). The ringlet's e' then grows over time (orange, green, red curves), which reverses the sign of $\partial\omega/\partial r$ near periapse when $e' > 0.75$; here the inner ringlet's angular speed is slower than the outer ringlet, and viscous friction causes angular momentum to instead flow inwards at these longitudes. Dashed curve is Eqn. (A1) with $e' = \sqrt{3}/2$ and assuming $|\tilde{\omega}'| \ll 1$.

at longitudes nearer periapse where $|\varphi| \sim 0$, and outwards at all other longitudes, with that flux reversal being due to the reversal of the ringlet's angular velocity gradient, Fig. 9. Figure 13 also shows that the ringlet's gravitational transport of angular momentum is inwards as ring-matter approaches periapse where $\varphi < 0$, and is outwards $\mathcal{F}_{L,g}(\varphi) > 0$ post-periapse, with that asymmetry being due to the ringlet's negative periapse twist, $\tilde{\omega}' < 0$ (Fig. 8).

Figure 14 shows the ringlet's energy fluxes due to viscosity (blue curve) and gravity (orange) at simulation end. Integrating these fluxes about a streamline's circumference at various times t then yields the the ringlet's viscous $\mathcal{L}_{E,\nu}$ and gravitational energy luminosity $\mathcal{L}_{E,g}$ over time, Fig. 15, where the gravitational energy luminosity is computed via

$$\mathcal{L}_{E,g}(a) = \oint \mathcal{F}_{E,g}(\varphi) r d\varphi = \oint \lambda r \mathbf{A}_g^1 \cdot \mathbf{v} d\varphi \quad (17)$$

where $\mathbf{A}_g^1$ is the one-sided gravitational acceleration experienced by a particle in streamline a. Note that even though $\mathcal{F}_{E,\nu}$ and $\mathcal{F}_{E,g}$ have very different spatial dependances (see Fig. 14), the influence of the ringlet's viscosity and gravity still conspire such that their orbit-integrated luminosities $\mathcal{L}_E = \oint(\mathcal{F}_{E,\nu} + \mathcal{F}_{E,g}) r d\varphi$ are zero once the ringlet has settled into the self-confining state.

Note that Fig. 15 also shows that the ringlet's gravitational energy luminosity is zero. Which is to be expected since the streamlines' gravitating ellipses only interact via their secular perturbations,

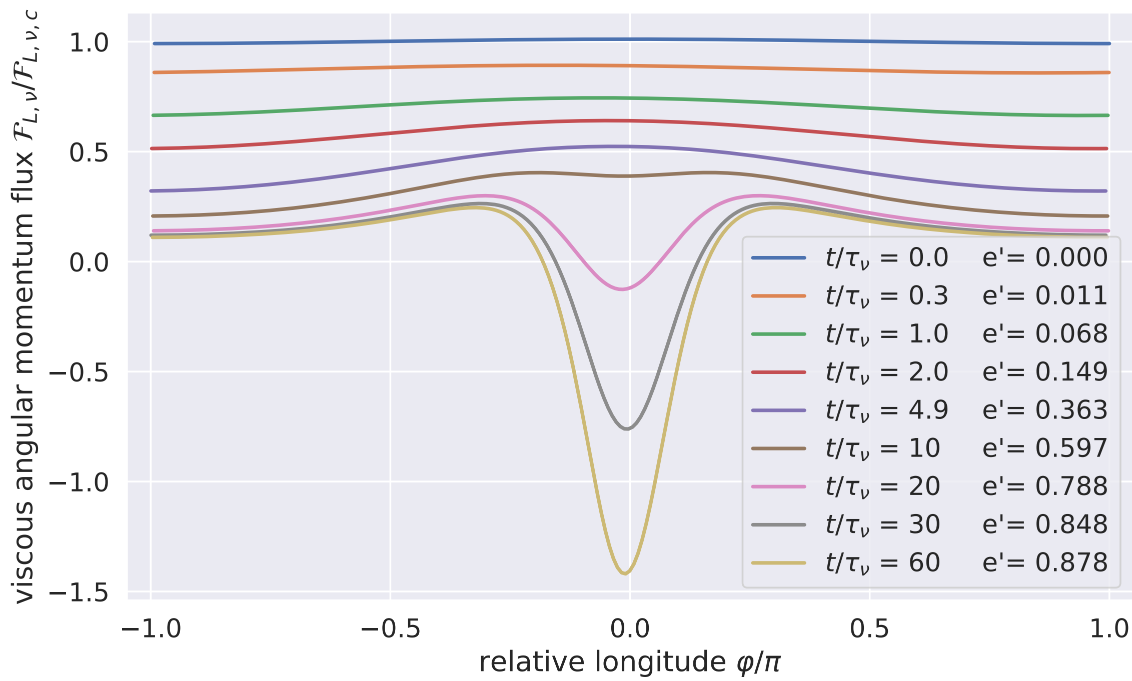

Figure 10. The nominal ringlet's viscous angular momentum flux $\mathcal{F}_{L,\nu}(\varphi)$, Eqn. (15), is plotted versus ringlet relative longitude $\varphi = \theta - \tilde{\omega}$ about the ringlet's inner streamline at selected times t/τ_ν, with the ringlet's eccentricy gradient e' also indicated, and $\mathcal{F}_{L,\nu,c}$ the angular momentum flux in a circular ringlet

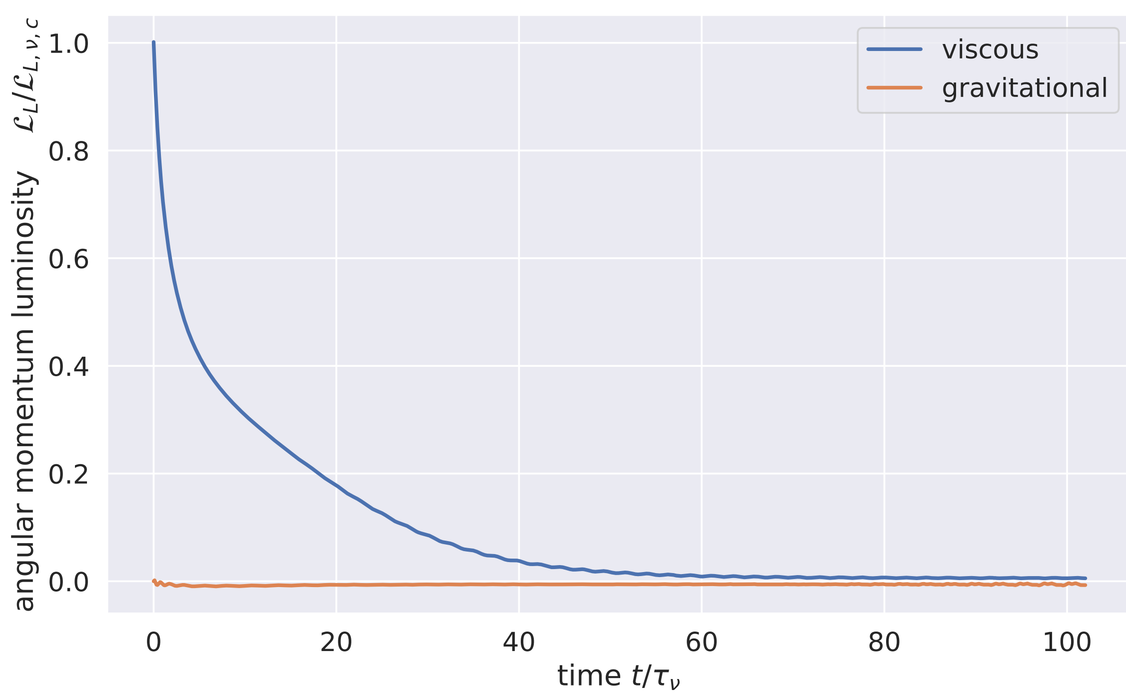

Figure 11. Nominal ringlet's viscous angular momentum luminosity $\mathcal{L}_{L,\nu}$ (blue curve) versus time t/τ_ν and in units of a circular ring's viscous angular momentum luminosity $\mathcal{L}_{L,\nu,c}$, as well as the ringlet gravitational angular momentum luminosity $\mathcal{L}_{L,g}$ (orange curve).

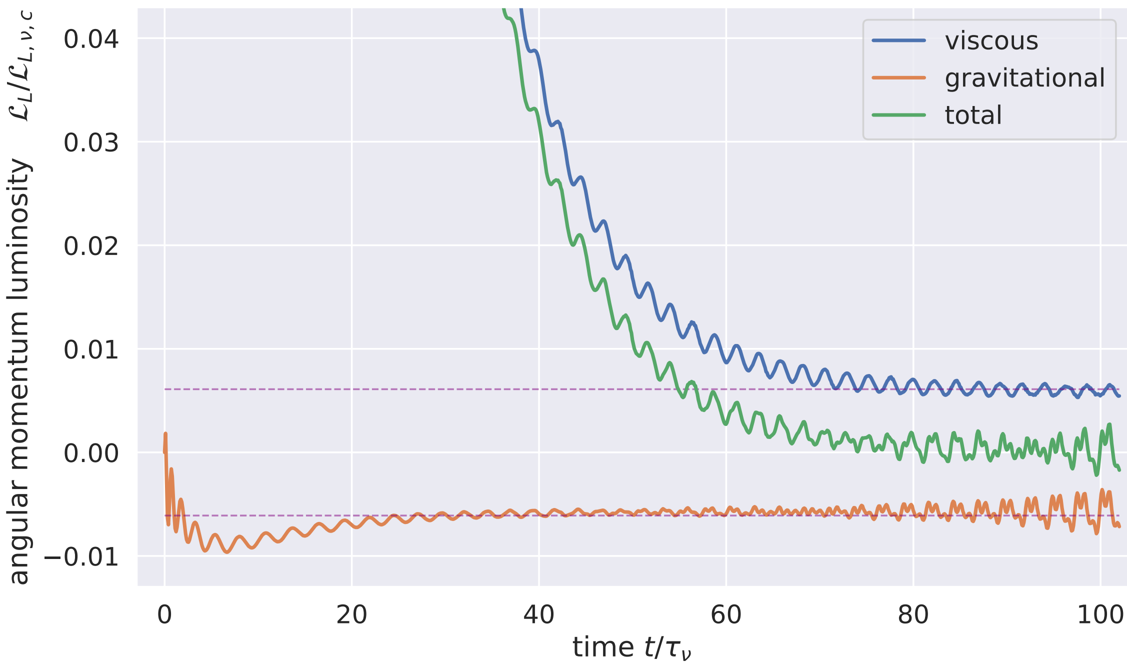

Figure 12. Figure 11 is replotted to show that the ringlet's viscous angular momentum luminosity $\mathcal{L}_{L,\nu}$ (blue curve) always stays positive (indicating that the viscous transport of angular momentum is radially outwards) and is eventually balanced by the ringlet's negative (*i.e.* inwards) gravitational angular momentum luminosity $\mathcal{L}_{L,g}$ (orange) after time $t \geq 80\tau_\nu$. Green curve is total angular momentum luminosity $\mathcal{L}_{L,\nu}+\mathcal{L}_{L,g}$ whose time-average is zero when $t \geq 80\tau_\nu$.

and secular perturbations do no work (Brouwer & Clemence 1961), hence $\mathcal{L}_{E,g} = 0$. That this quantity evaluates to zero within $\pm 5 \times 10^{-24}$ (in nautural units) can also be regarded as another test of the epi_int_lite integrator's numerical quality.

4.5. *variations with ringlet width, mass, and viscosity*

To assess whether the nominal ringlet's evolution is typical of other ringlets having alternate values of initial width Δa, total mass m_r, and shear viscosity ν_s, a survey of 1154 additional ringlet simulations are executed. The survey ringlets are similar to the nominal ringlet with $N_s = 2$ streamlines having $N_p = 241$ particles per streamline, initial eccentricity $e = 0.01$, initial eccentricity gradient $e' = 0$, and viscosities $\nu_b = \nu_s$. But the survey ringlets instead have total masses that are geometrically distributed between $1.3 \times 10^{-10} \leq m_r \leq 1.3 \times 10^{-8}$, shear viscosities geometrically distributed between $3.1 \times 10^{-13} \leq \nu_s \leq 3.1 \times 10^{-10}$, and initial radial widths linearly distributed between $0.0003 \leq \Delta a \leq 0.0016$. Survey results are summarized in Fig. 16 where blue, green and orange squares indicate those ringlets did evolve into a self-confining state, with pink diamonds to indicate those simulations described below as "partially confined".

Five panels are shown in Fig. 16, one for each value of initial Δa, and the colored squares in these panels show that there is a single island in the three-dimensional $(\Delta a, m_r, \nu_s)$ parameter space where survey simulations do evolve into the self-confining state. Blue squares represent those ringlets that settle into self-confinement with low libration amplitudes, and these ringlets have a nonlinear parameter q that varies by no more than $\Delta q \leq 6 \times 10^{-4}$ as the ringlet librates about equilibrium

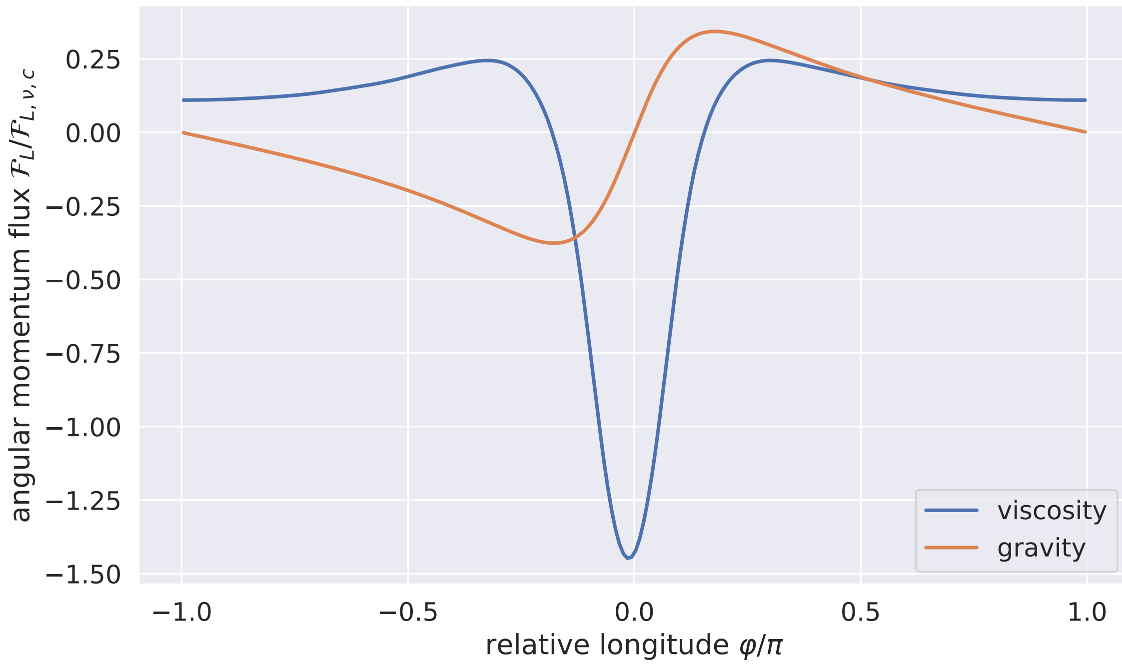

Figure 13. The nominal ringlet's viscous angular momentum flux $\mathcal{F}_{L,\nu}(\varphi)$ (blue curve) is computed via Eqn. (3) and plotted in units of a circular ringlet's flux $\mathcal{F}_{L,\nu,c}$ versus relative longitude φ at the simulation's end time $t = 100\tau_\nu$, as well as the ringlet's gravitational angular momentum flux $\mathcal{F}_{L,g}(\varphi)$ (orange curve via Eqn. 10).

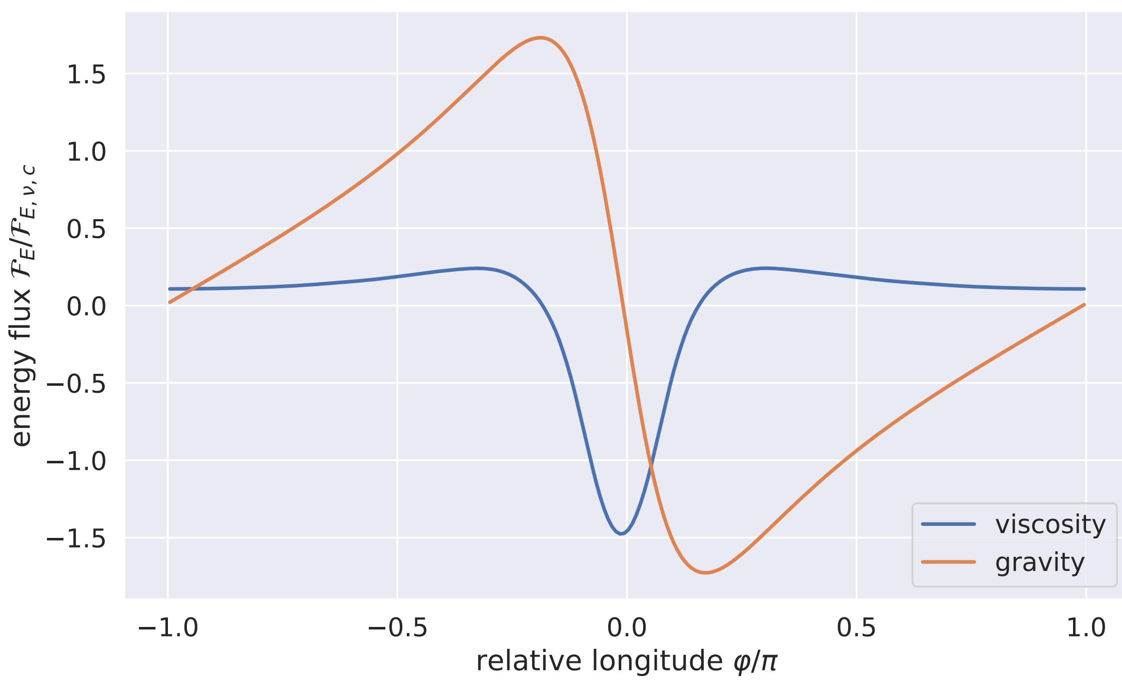

Figure 14. Blue curve is the nominal ringlet's viscous energy flux $\mathcal{F}_{E,\nu}(\varphi)$, plotted in units of a circular ringlet's viscous energy flux $\mathcal{F}_{E,\nu,c}$ and versus the ringlet's relative longitude φ at the simulation's end time $t = 100\tau_\nu$, as well as the ringlet's gravitational energy flux $\mathcal{F}_{E,g}(\varphi)$.

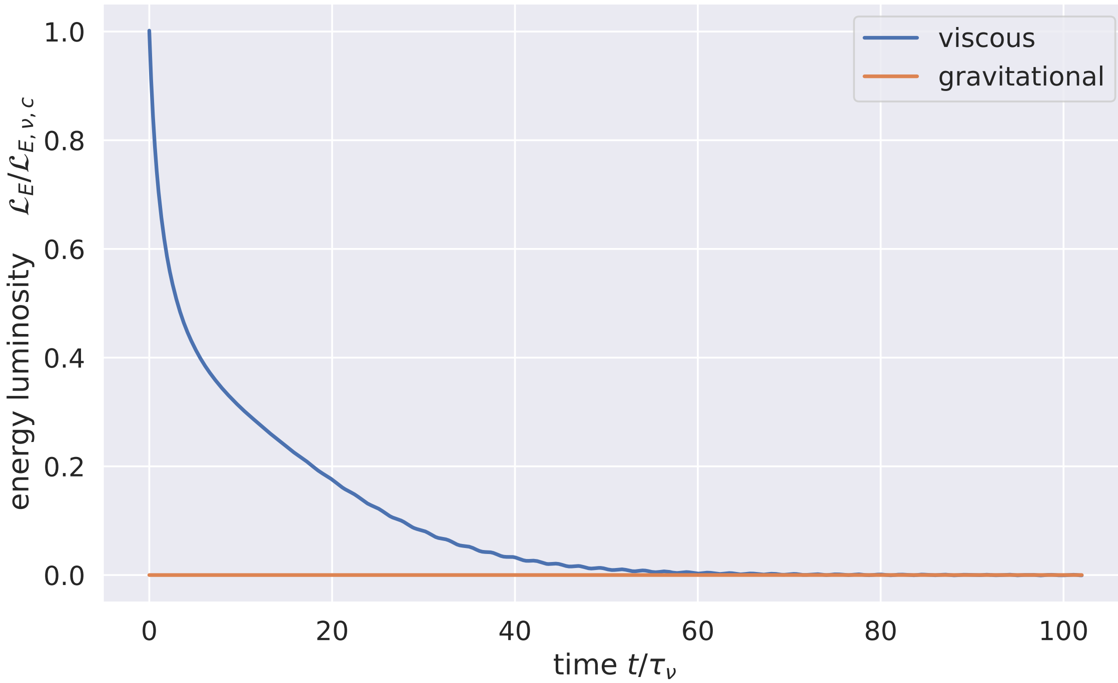

Figure 15. Nominal ringlet's viscous energy luminosity $\mathcal{L}_{E,\nu}$ (blue curve) versus time t/τ_ν and in units of a circular ring's viscous energy luminosity $\mathcal{L}_{E,\nu,c}$, as well as the ringlet gravitational energy luminosity $\mathcal{L}_{E,g}$ (orange curve).

during the simulation's final 20%. Green squares indicated those ringlets that are librating with higher amplitudes, $6 \times 10^{-4} < \Delta q \leq 4 \times 10^{-3}$, after settled into self-confinement, while orange squares indicate those self-confining ringlets that are most disturbed, with $\Delta q > 4 \times 10^{-3}$.

Pink diamonds indicate simulations that are "partially" confined, these ringlets do achieve a high $q \sim 0.9$, but angular momentum flux reversal is not complete and so their viscous spreading is only slowed not stalled, which is also detailed in the lowest row of plots in Fig. 17.

The × simulations in Fig. 16 terminated early when an epi_int_lite particle crossed a neighboring streamline. In reality, strong pressure forces would have developed as adjacent streamlines converged and enhanced particle densities and particle collisions, with ring particles possibly rebounding off this high-density region and/or splashing vertically, none of which is accounted for with this version of epi_int_lite. So this survey simply terminates all such simulations and flags that occurrence with an × in Fig. 16. Keep in mind though that this does not mean that these particular ringlets would not evolve into a self-confining state. Instead, the streamlines in these ringlets would evolve so close to each other that a more sophisticated and possibly nonlinear treatment of pressure effects is needed to accurately assess these ringlets' fates.

The black numbers in Fig. 16 are the IDs of a selection of ringlet simulations that settle into full or partial self-confinement, and the time-histories of those ringlets are shown in Fig. 17. Each row of plots there shows the time-evolution of the ringlets' nonlinear parameter q, semimajor axis width Δa, and eccentricity e for ringlets having the same or similar mass m_r and viscosity ν_s. The libration amplitudes Δq that are indicated in Fig. 16 via color-coded squares are simply the q variations observed in the final 20% of the evolutions seen in Fig. 17. The lowest row of plots in Fig. 17 show

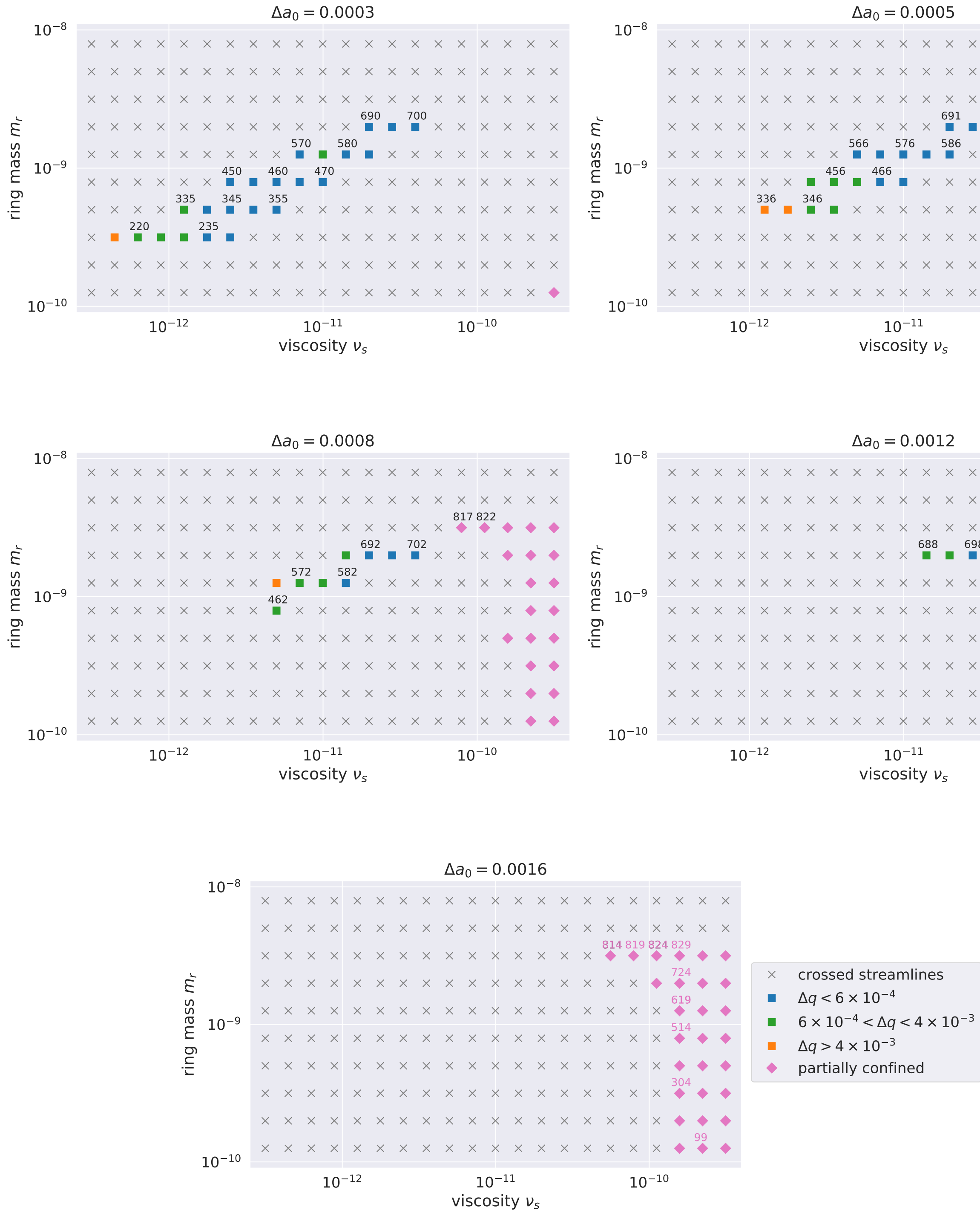

Figure 16. Outcomes for 1155 ringlet simulations having a variety of ringlet masses m_r, shear viscosities ν_s, with each panel showing results for ringlets having the same initial radial width, $\Delta a = 0.0003, 0.0005, 0.0008, 0.0012,$ or 0.0016. Colored squares indicate those ringlets that evolve into the self-confining state with the indicated libration amplitudes Δq, pink diamonds for those simulations that are partially confined, and $\times$ for simulations that terminate early when an epi_int_lite particle crossed an adjacent streamline. Black numbers indicate the IDs of selected simulations whose time-evolution are shown in Fig. 17, and the nominal ringlet simulation has ID=345. Pink IDs indicate selected partially confined ringlet simulations whose evolutions are also plotted in Fig. 19.

the evolutions of the partially-confined ringlet simulations that are indicated by pink squares in Fig. 16, that row shows that though these simulations have nonlinearity parameters that do exceed the theoretical $q = \sqrt{3}/2$ limit expected for self-confinement, those ringlets' Δa still slowly spread and thus are designated "partially" confined. Close inspection of the Δa curves in the row above show that those ringlets' semimajor axes also spread albeit more slowly. So it is probably safer to say that the simulations in the upper rows of Fig. 17 are more self-confining that those in the lower rows.

The quantities shown in Fig. 17 are plotted versus t/τ_{dyn} where τ_{dyn} is the simulated ringlet's dynamical timescale

$$\tau_{dyn} = \tau_{\nu,n} \left(\frac{m_r}{m_{r,n}}\right)^{\alpha} \left(\frac{\nu_s}{\nu_{s,n}}\right)^{\beta} \left(\frac{\Delta a}{\Delta a_n}\right)^{\gamma}, \tag{18}$$

which is assumed to be a power-law in the ringlet's physical properties m_r, ν_s, Δa, where $m_{r,n} = 5 \times 10^{-10}$ is the nominal ringlet's mass, $\nu_{s,n} = 2.5 \times 10^{-12}$ is the nominal ringlet's shear viscosity, $\Delta a_n = 3 \times 10^{-4}$ is the nominal ringlet's initial semimajor axis width, and $\tau_{\nu,n} = 3 \times 10^{3}$ is the nominal ringlet's viscous timescale, Eqn. (7). The exponents in Eqn. (18) are $\alpha = 0.5$, $\beta = -0.5$, $\gamma = 0.0$, and are chosen so that the q versus t/τ_{dyn} curve for all simulations in Fig. 17 overlaps as much as possible, as seen in Fig. 18. Equation (18) is used here to anticipate execution times for the various simulations shown in Fig. 16, which varies by a factor of ~ 500, and all simulations shown in Figs. 16–20 are evolved for the greater of $10\tau_{dyn}$ or $10\tau_{\nu}$.

4.5.1. *partial self–confinement*

The evolution of a selection of partially self confined ringlet simulations, as well as the nominal ringlet whose ID=345, are also shown in Fig. 19, which plots ringlet's eccentricity gradient e' versus time t/τ_{dyn}. All of these ringlets achieve nonlinearity parameters $q \simeq \sqrt{3}/2 \simeq 0.866$ after time $t \gtrsim$ a few τ_{dyn}, but these ringlets' eccentricity gradients are significantly less than the theoretical $e' \simeq 0.866$ limit (dotted red curve). In fact the range of simulated ringlet's e' almost spans the entire range of eccentricity gradients observed among Saturn's most well-studied narrow eccentric ringlets, the Maxwell, Titan, Laplace, and Huygens ringlets, whose e' are indicated by the black horizontal lines in Fig. 19. Also keep in mind that Fig. 19 is not an apples-to-apples comparison of simulated ringlets to observed ringlets, since the simulations reported in Fig. 19 all have a common semimajor axis width Δa, eccentricity e_0, and very similar viscosities ν_s, whereas the observed ringlets have a spectrum of physical properties (e_0, Δa, m_r, ν_s). The main point of Fig. 19 is that, if the known narrow eccentric ringlets are in fact self-confining, then they are of the partially self confined variety, which means that they have a nonlinearity parameter $q \simeq \sqrt{3}/2 \simeq 0.866$, an eccentricity gradient e' that is significantly less than 0.866, as well as a periapse twist $|\tilde{\omega}'|$ that is not negligable per Eqn. (9).

Section 4.6 will derive the rate at which a self-confining ringlet's eccentricity e decays over time due to viscosity, Eqns. (24–25), and all ringlets shows in Figs. 17–19, which includes fully as well as partially self-confining ringlets, all have eccentricities e that decay at the expected rates.

4.5.2. *variations with ringlet viscosity*

Figure 20 shows the periapse twist $\tilde{\omega}' \simeq ea\Delta\tilde{\omega}/\Delta a$ versus time for five ringlets having the same initial e_0, Δa, and m_r as the nominal ringlet but differing viscosities ν_s, and that plot shows that twist $|\tilde{\omega}'|$ varies with ν_s. Which indicates that if the twist $|\tilde{\omega}'|$ could be observed in a self-confining ringlet, then the ringlet's viscosity could then be inferred.

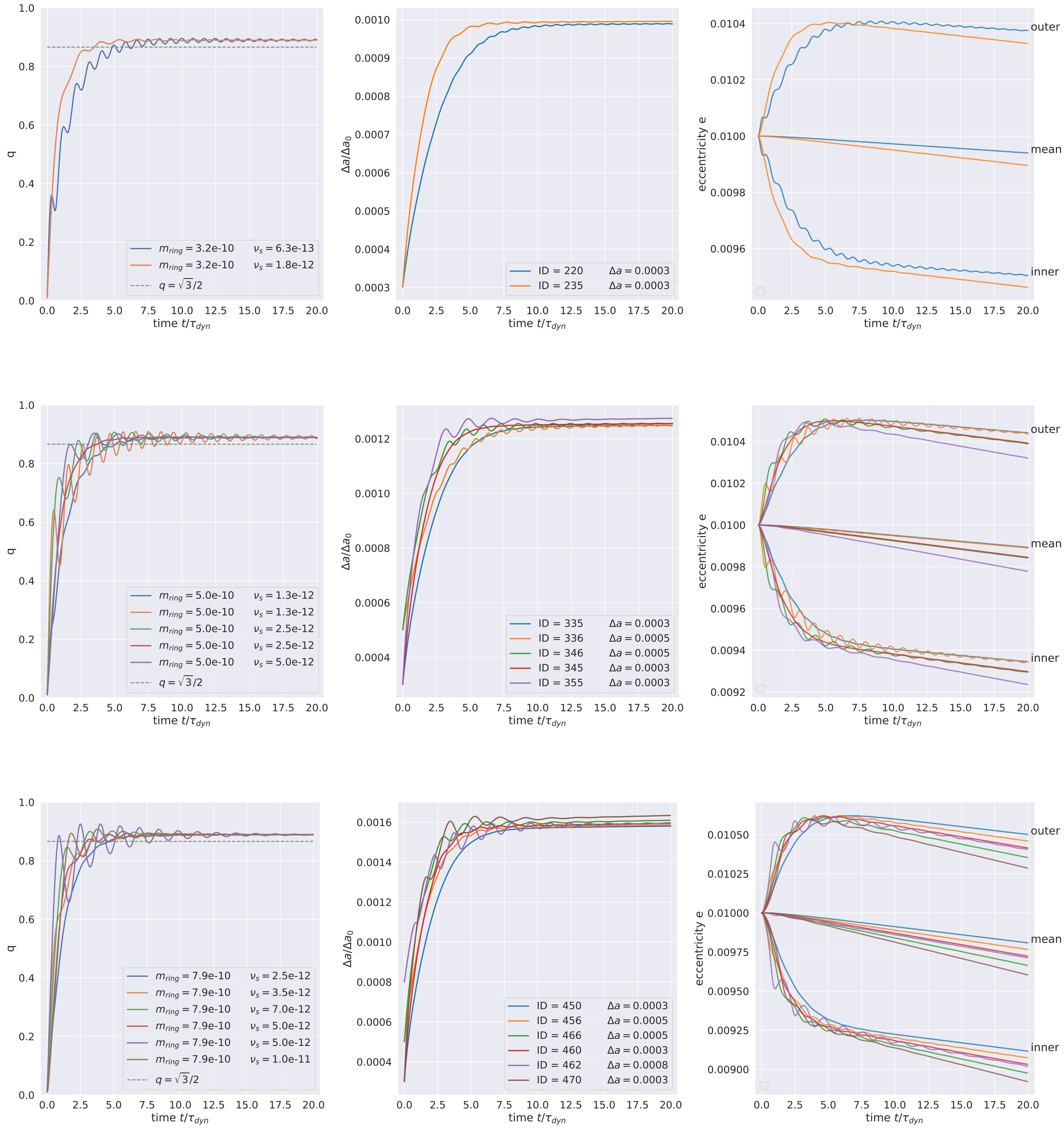
q
time t/τ_{dyn}
$m_{ring} = 3.2\text{e-}10$ $\nu_s = 6.3\text{e-}13$
$m_{ring} = 3.2\text{e-}10$ $\nu_s = 1.8\text{e-}12$
$q = \sqrt{3}/2$
$\Delta a/\Delta a_0$
ID = 220 $\Delta a = 0.0003$
ID = 235 $\Delta a = 0.0003$
eccentricity e
outer
mean
inner
$m_{ring} = 5.0\text{e-}10$ $\nu_s = 1.3\text{e-}12$
$m_{ring} = 5.0\text{e-}10$ $\nu_s = 1.3\text{e-}12$
$m_{ring} = 5.0\text{e-}10$ $\nu_s = 2.5\text{e-}12$
$m_{ring} = 5.0\text{e-}10$ $\nu_s = 2.5\text{e-}12$
$m_{ring} = 5.0\text{e-}10$ $\nu_s = 5.0\text{e-}12$
$q = \sqrt{3}/2$
ID = 335 $\Delta a = 0.0003$
ID = 336 $\Delta a = 0.0005$
ID = 346 $\Delta a = 0.0005$
ID = 345 $\Delta a = 0.0003$
ID = 355 $\Delta a = 0.0003$
$m_{ring} = 7.9\text{e-}10$ $\nu_s = 2.5\text{e-}12$
$m_{ring} = 7.9\text{e-}10$ $\nu_s = 3.5\text{e-}12$
$m_{ring} = 7.9\text{e-}10$ $\nu_s = 7.0\text{e-}12$
$m_{ring} = 7.9\text{e-}10$ $\nu_s = 5.0\text{e-}12$
$m_{ring} = 7.9\text{e-}10$ $\nu_s = 5.0\text{e-}12$
$m_{ring} = 7.9\text{e-}10$ $\nu_s = 1.0\text{e-}11$
$q = \sqrt{3}/2$
ID = 450 $\Delta a = 0.0003$
ID = 456 $\Delta a = 0.0005$
ID = 466 $\Delta a = 0.0005$
ID = 460 $\Delta a = 0.0003$
ID = 462 $\Delta a = 0.0008$
ID = 470 $\Delta a = 0.0003$

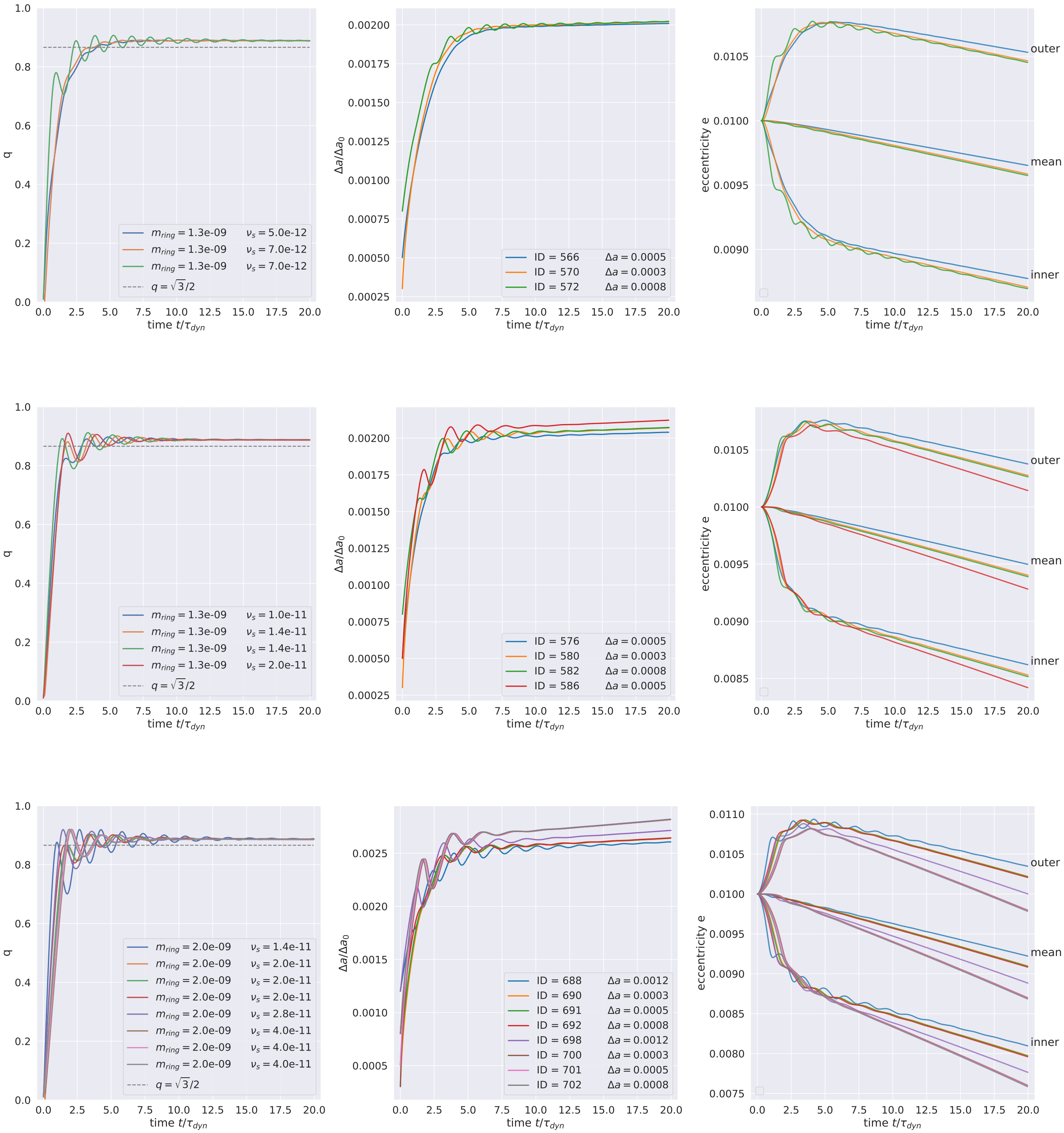
q
time t/τ_{dyn}
$m_{ring} = 1.3e\text{-}09$ $\nu_s = 5.0e\text{-}12$
$m_{ring} = 1.3e\text{-}09$ $\nu_s = 7.0e\text{-}12$
$m_{ring} = 1.3e\text{-}09$ $\nu_s = 7.0e\text{-}12$
$q = \sqrt{3}/2$
$\Delta a/\Delta a_0$
ID = 566 $\Delta a = 0.0005$
ID = 570 $\Delta a = 0.0003$
ID = 572 $\Delta a = 0.0008$
eccentricity e
outer
mean
inner
$m_{ring} = 1.3e\text{-}09$ $\nu_s = 1.0e\text{-}11$
$m_{ring} = 1.3e\text{-}09$ $\nu_s = 1.4e\text{-}11$
$m_{ring} = 1.3e\text{-}09$ $\nu_s = 1.4e\text{-}11$
$m_{ring} = 1.3e\text{-}09$ $\nu_s = 2.0e\text{-}11$
ID = 576 $\Delta a = 0.0005$
ID = 580 $\Delta a = 0.0003$
ID = 582 $\Delta a = 0.0008$
ID = 586 $\Delta a = 0.0005$
$m_{ring} = 2.0e\text{-}09$ $\nu_s = 1.4e\text{-}11$
$m_{ring} = 2.0e\text{-}09$ $\nu_s = 2.0e\text{-}11$
$m_{ring} = 2.0e\text{-}09$ $\nu_s = 2.0e\text{-}11$
$m_{ring} = 2.0e\text{-}09$ $\nu_s = 2.0e\text{-}11$
$m_{ring} = 2.0e\text{-}09$ $\nu_s = 2.8e\text{-}11$
$m_{ring} = 2.0e\text{-}09$ $\nu_s = 4.0e\text{-}11$
$m_{ring} = 2.0e\text{-}09$ $\nu_s = 4.0e\text{-}11$
$m_{ring} = 2.0e\text{-}09$ $\nu_s = 4.0e\text{-}11$
ID = 688 $\Delta a = 0.0012$
ID = 690 $\Delta a = 0.0003$
ID = 691 $\Delta a = 0.0005$
ID = 692 $\Delta a = 0.0008$
ID = 698 $\Delta a = 0.0012$
ID = 700 $\Delta a = 0.0003$
ID = 701 $\Delta a = 0.0005$
ID = 702 $\Delta a = 0.0008$

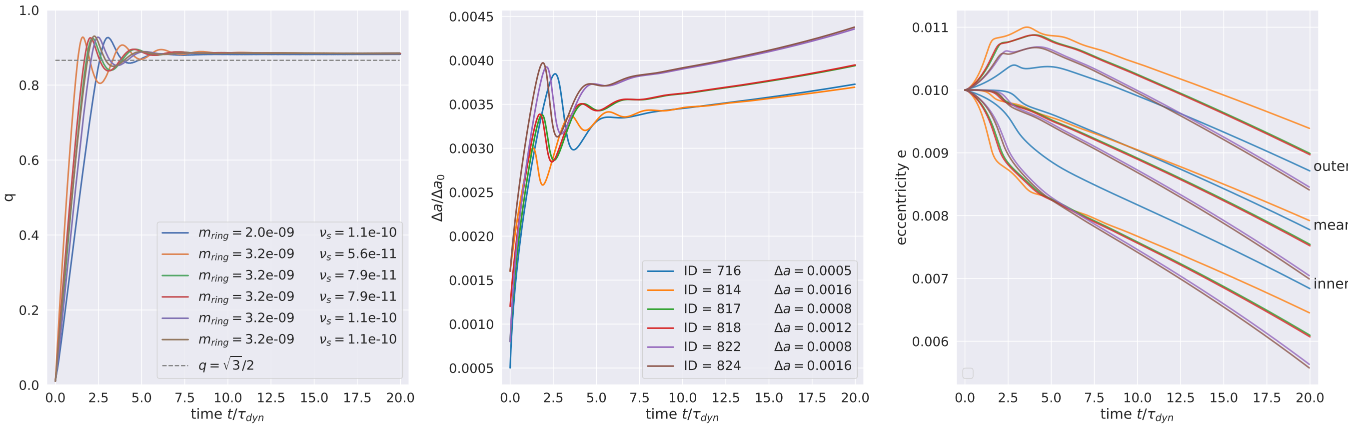

Figure 17. Each row of plots shows ringlets' nonlinear parameter q (left plot), semimajor axis width Δa (middle plot), and streamline's outer, mean, and inner eccentricities e (right plot) versus time t for ringlets having the same or similar mass m_r and viscosity ν_s, for each simulation whose black IDs are indicted in Fig. 16. All quantities are plotted versus t/τ_{dyn} where each ringlet's dynamical timescale τ_{dyn} is Eqn. (18).

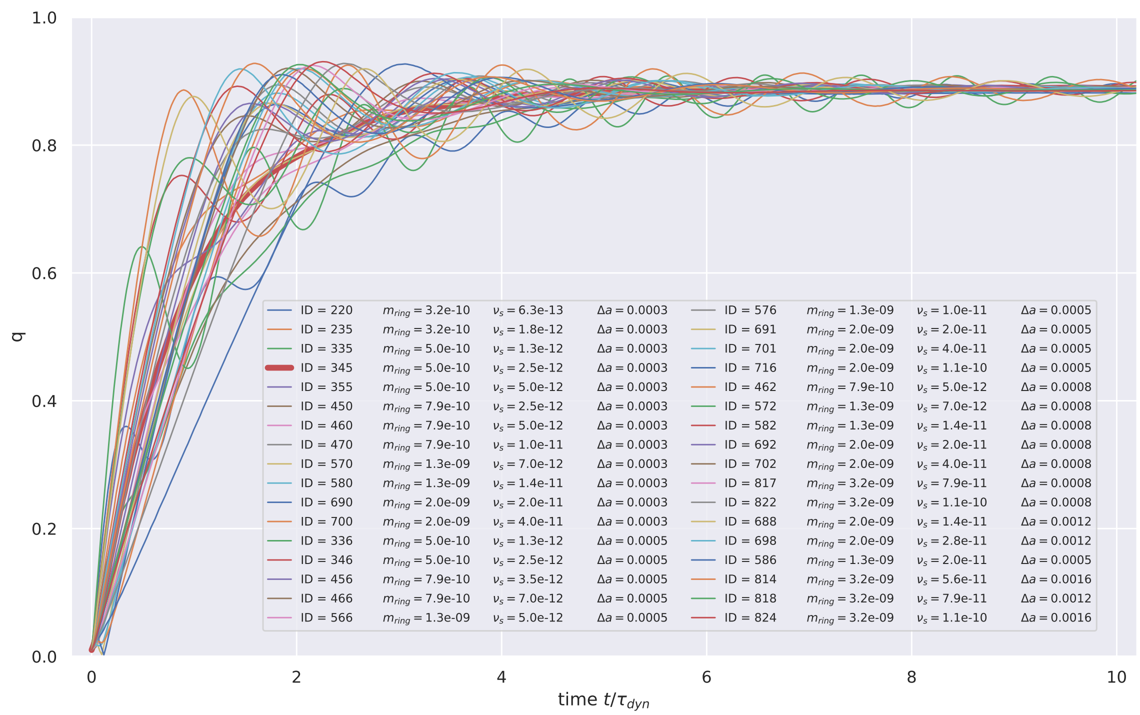

Figure 18. Nonlinear parameter q is plotted versus time for each of the simulations indicated by black IDs in Figs. 16 and 17, with time t scaled by each ringlet's empirical dynamical timescale τ_{dyn}, Eqn. (18). Thick red curve shows the evolution of the nominal ringlet whose ID=345. All other ringlet trajectories are distributed about the nominal ringlet's trajectory, which indicates that Eqn. (18) is an adequate estimator of a ringlet's dynamical evolution timescale when $\alpha = 0.5$, $\beta = -0.5$, $\gamma = 0.0$.

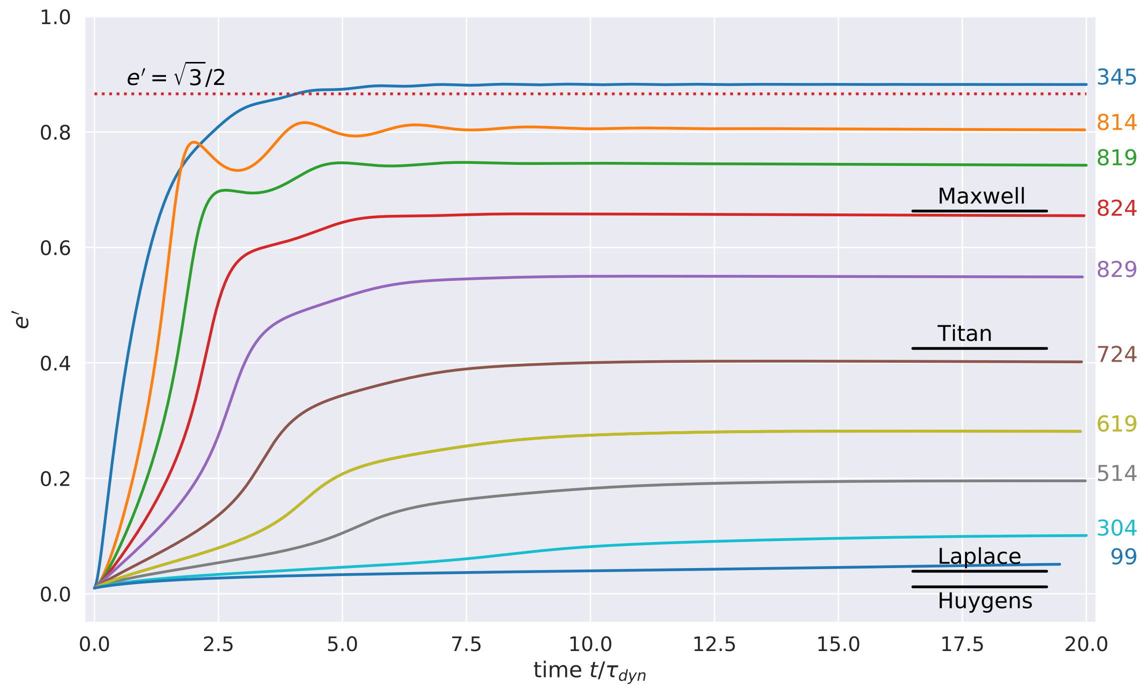

Figure 19. Eccentricity gradient e' versus time t/τ_{dyn} for selected partially self-confining ringlets whose simulation IDs are indicated on the right of this Figure and as pink text in Fig. 16. Black horizontal lines show e' for Saturn's Maxwell, Titan, Laplace, and Huygens ringlets (references?), and the dotted line indicates the $e' = \sqrt{3}/2$ threshold.

4.5.3. *variations with initial eccentricity*

Additional simulations are used to assess how outcomes depend upon the ringlet's initial eccentricity e_0. Figure 21 shows seven simulations of the nominal ringlet that all have identical physical properties (mass, initial width Δa) but differing initial e_0 ranging over $0 \leq e_0 \leq 0.025$, and two types of outcomes are observed. Higher e_0 simulations having $e_0 \gtrsim 0.005$ evolve into the self-confining state with $q \simeq \sqrt{3}/2$ and constant width Δa (e.g. the lower purple, brown and dark-blue curves). However lower $e_0 \lesssim 0.005$ (red, green, orange) simulations are only are partially self–confining in that self-gravity does not pump up the ringlet's q sufficient for self-confinement, so these simulated ringlet's Δa spreads radially albeit slower than the circular ringlet (uppermost blue curve). This bifurcated outcome suggest that the nominal ringlet has a separatrix that divides true self-confinement (which requires $e_0 \gtrsim 0.005$) from partial or no confinement. This in turn suggests that the partially confined ringlet's (pink diamonds) seen in Fig. 16 might instead have achieved true confinement had they started with sufficiently high initial e_0.

4.6. *eccentricity damping*

Viscous friction within the ringlet is a result of dissipative collisions among ringlet particles. Particle collisions generate heat that is radiated into space, and the source of that radiated energy is the ringlet's orbital energy $E_r = -m_r GM/2a + E_{sg}$ where m_r is the ringlet's total mass, a its semimajor axis, and E_{sg} is the ringlet's energy due to its self gravity which is contant when the ringlet is self-confining. Collisions conserve angular momentum, so the ringlet's total angular momentum

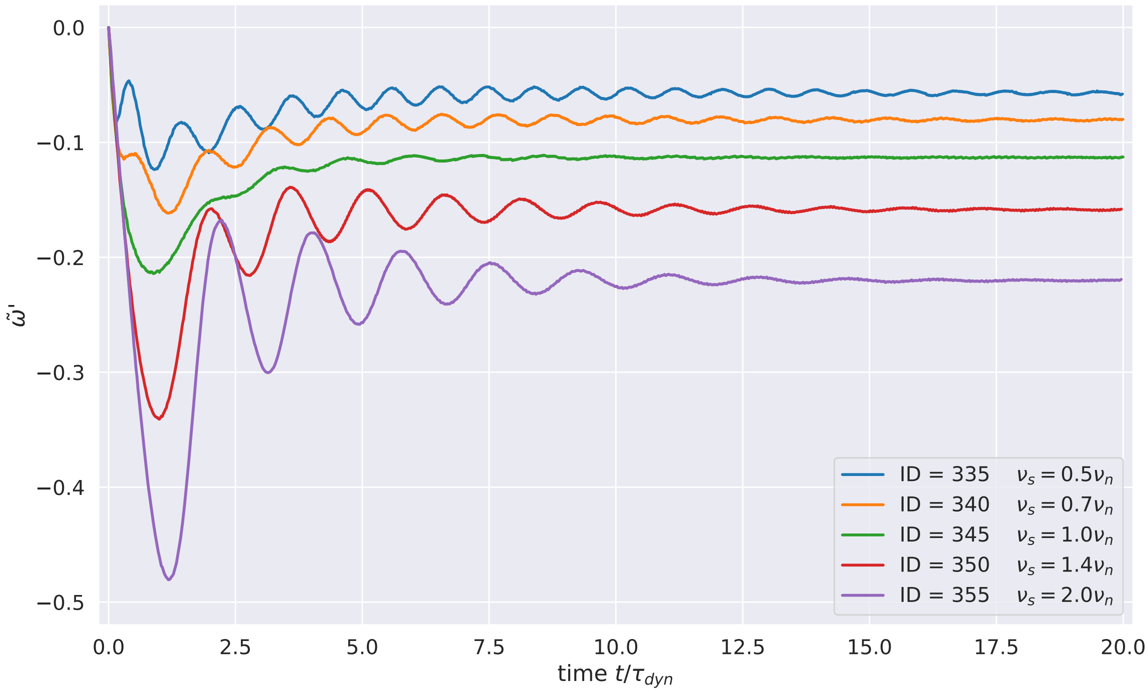

Figure 20. Periapse twist $\tilde{\omega}'$ is plotted versus time t/τ_ν for five ringlets having the same initial e_0, Δa, m_r as the nominal ringlet (whose simulation ID=345) but differing viscosities ν_s that range over $0.5\nu_n \le \nu_s \le 2\nu_n$ where $\nu_n = 2.5 \times 10^{-12}$ is the nominal ringlet's shear visocity.

$L_r = m_r\sqrt{GMa(1-e^2)}$ is constant so $dL_r/dt = 0$ implies

$$\frac{de^2}{dt} \simeq \frac{1}{a}\frac{da}{dt} \tag{19}$$

to lowest order in the ringlet's small eccentricity e. The ringlet's energy dissipation rate is $\dot{E}_r = dE_r/dt = m_r GM\dot{a}/2a^2$ so $\dot{a} \simeq 2\dot{E}_r/m_r a\Omega^2$ and

$$\frac{de^2}{dt} \simeq \frac{2\dot{E}_r}{m_r a^2\Omega^2} \tag{20}$$

where $GM \simeq a^3\Omega^2$ to lowest order in J_2. Also note that the surface area of energy dissipation within a viscous disk is

$$\delta = -\nu_s\sigma(r\omega')^2 \tag{21}$$

(Pringle 1981 I think) where $\omega = v_\theta/r$ is the angular velocity and $\omega' = \partial\omega/\partial r$ its radial gradient.

Now consider a small tangential segment within the ringlet whose length is $d\ell = rd\varphi$ where φ is the segment's longitude measured from the ringlet's periapse and $d\varphi$ is the small segment's angular extent. The segment's area is $dA = \Delta r d\ell = r\Delta r d\varphi$ where Δr is the ringlet's radial width. The rate at which that patch's viscosity dissipates orbital energy is $d\dot{E}_r = \delta dA$, so the ringlet's total energy dissipation rate is $\dot{E}_r = \oint d\dot{E}_r$ when integrated about the ringlet's circumference, and so $\dot{E}_r = -2\nu_s\lambda\int_0^\pi r^3\omega'^2 d\varphi$ since the ringlet's linear density $\lambda = \sigma\Delta r \simeq m_r/2\pi a$. So the total energy loss rate due to ringlet viscosity becomes

$$\dot{E}_r \simeq -\frac{9}{4}I(e')m_r\nu_s\Omega^2 \tag{22}$$

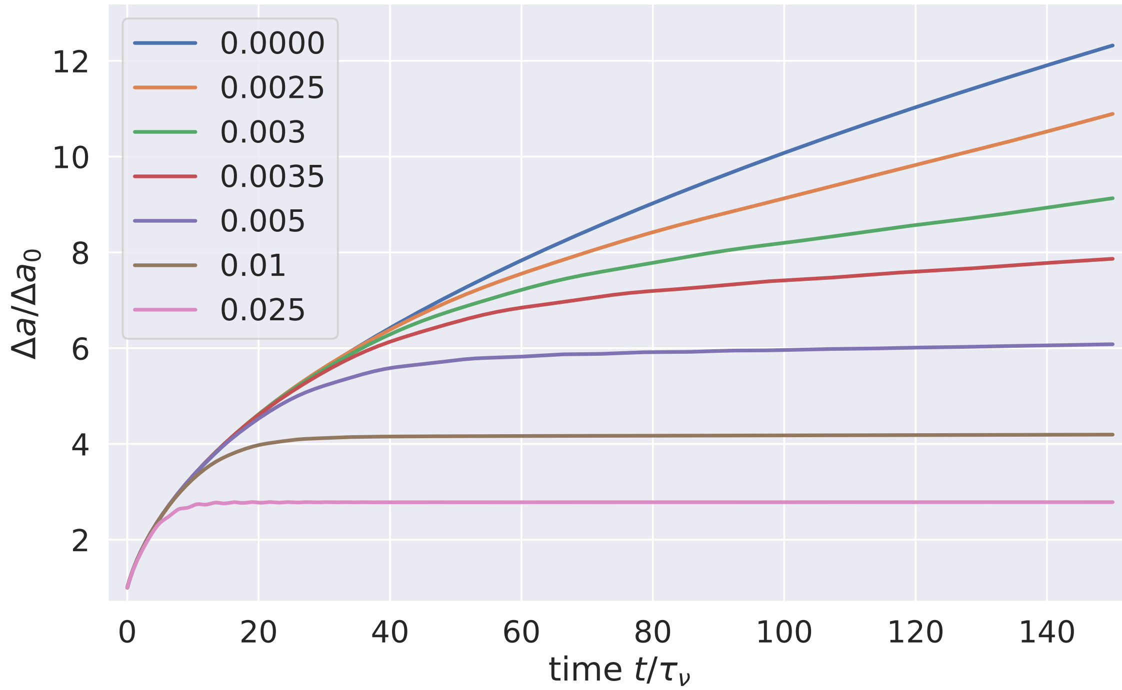

Figure 21. Simulations of seven nominal ringlets having a variety of initial eccentricities $0 \le e_0 \le 0.025$. Plot shows each ringlet's semimajor axis width Δa in units of its initial Δa_0 versus time t/τ_ν, and simulations having higher initial $e_0 \gtrsim 0.005$ (lower purple, brown and dark-blue curves) evolve into the self-confining state with nonlinearity parameter $q \simeq \sqrt{3}/2$. Ringlets having lower initial $e_0 \lesssim 0.005$ (red, green, and orange curves) are partially self-confining, while the $e_0 = 0$ ringlet (upper blue curve) is always unconfined and experiences fastest radial spreading.

when Eqn. (A1) is used to replace ω', and the integral

$$I(e') = \frac{1}{\pi}\int_0^\pi \left(\frac{1-\frac{4}{3}e'\cos\varphi}{1-e'\cos\varphi}\right)^2 d\varphi. \tag{23}$$

Note that $I(e')$ is of order unity except when e' is very close to 1, and numerical evaluation shows that $I(e') \simeq 0.889$ when $e' = \sqrt{3}/2$.

Inserting Eqn. (22) into (20) then yields the rate at which e^2 is damped,

$$\frac{de^2}{dt} = -\frac{9I\nu_s}{2a^2} \tag{24}$$

which is easily integrated to obtain

$$e(t) = e_0\sqrt{1-\frac{t}{\tau_e}} \tag{25}$$

where e_0 is the ringlet's initial eccentricity and

$$\tau_e = \frac{2a^2e_0^2}{9I\nu_s} \tag{26}$$

is the ringlet's eccentricity damping timescale. These expectations are also confirmed in Fig. 22, which plots $e(t)/e_0$ versus time t/τ_e using Eqns. (25–26), for each of the numbered simulations seen in Figs. 16–18, with good agreement seen between theory and numerical simulation.

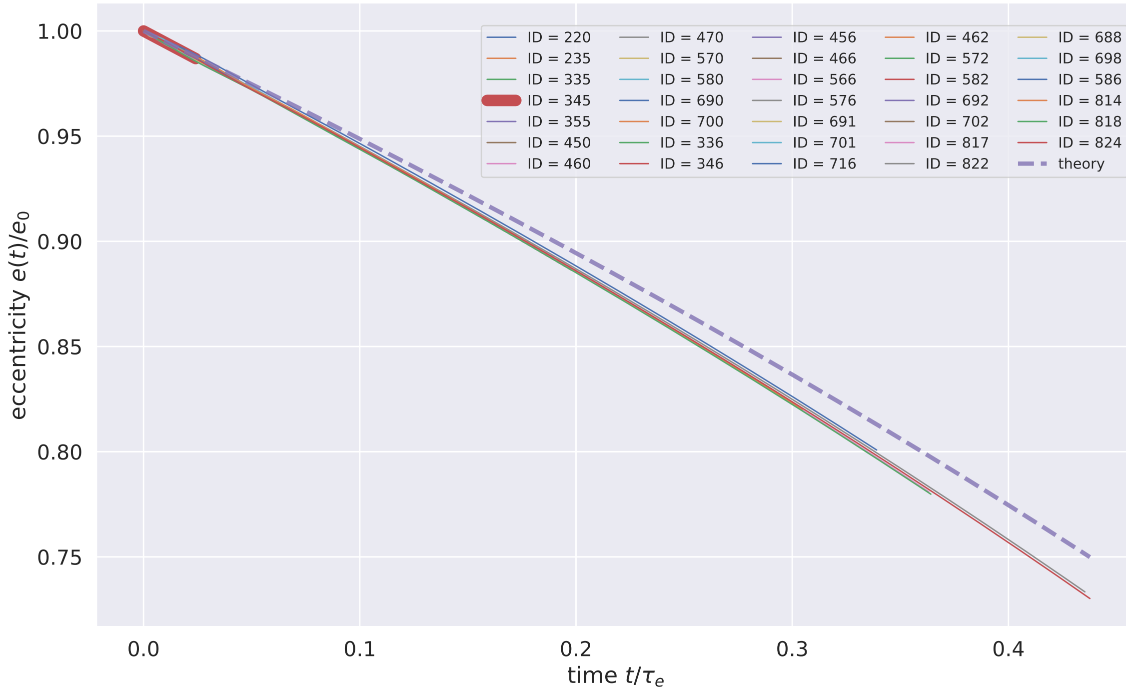

Figure 22. Plot of $e(t)/e_0$ versus time t/τ_e for each of the numbered simulations seen in Figs. 16–18, while the dashed curve is the expected behavior, Eqn. (25). These simulations have values of τ_e ranging over..., and thick red curve is the nominal ringlet whose ID=345.

So viscosity circularizes the ringlet in time τ_e, during which time the ringlet's semimajor axis will have shrunk by $\Delta a = \dot{a}\tau_e = -e_0^2 a$ by Eqns (19) and (24), so the ringlet's fractional drift inwards due to viscous damping is

$$\frac{\Delta a}{a} = -e_0^2, \tag{27}$$

which is small. And after the ringlet's inner edge damps to zero, its eccentricity gradient e' will then shrink over time, angular momentum flux reversal will diminish, and the ringlet's viscous spreading will resume. So self-confinement of narrow eccentric ringlets is only temporary after all, until time τ_e has elapsed, which is $\tau_e/2\pi \sim 1.6 \times 10^6$ orbits for the nominal model considered here, which is only $\sim 10^3$ years for a ringlet orbiting at $a \sim 10^{10}$ cm about Saturn. Recall from Section 3.1 that the viscous lifetime of a non-self-confining nominal ringlet is only $\tau_\nu/2\pi \sim 500$ orbits, so self-confinement evidently extends the lifetime of a narrow eccentric ringlet by factor of ~ 3000. But self-confinement does not solve the ringlet's lifetime problem, because self-confinement is ultimately defeated by viscous damping of the ringlet's eccentricity.

4.7. *number of streamlines N_s*

When the simulated ringlet is composed of $N_s = 2$ streamlines, the ringlet's evolution is largely analytic (*c.f.* Borderies et al. 1982, 1983), and those analytic predictions also provide excellent benchmark tests for the epi_int_lite integrator. This subsection assesses whether the results obtained for the simpler $N_s = 2$ ringlet also applies to more realistic ringlets having $N_s > 2$.

Figures 23–25 recompute the nominal ringlet's evolution but for ringlets having a range of streamlines, $2 \le N_s \le 31$. Figure 23 shows that ringlets having larger N_s also achieve larger semimajor axis

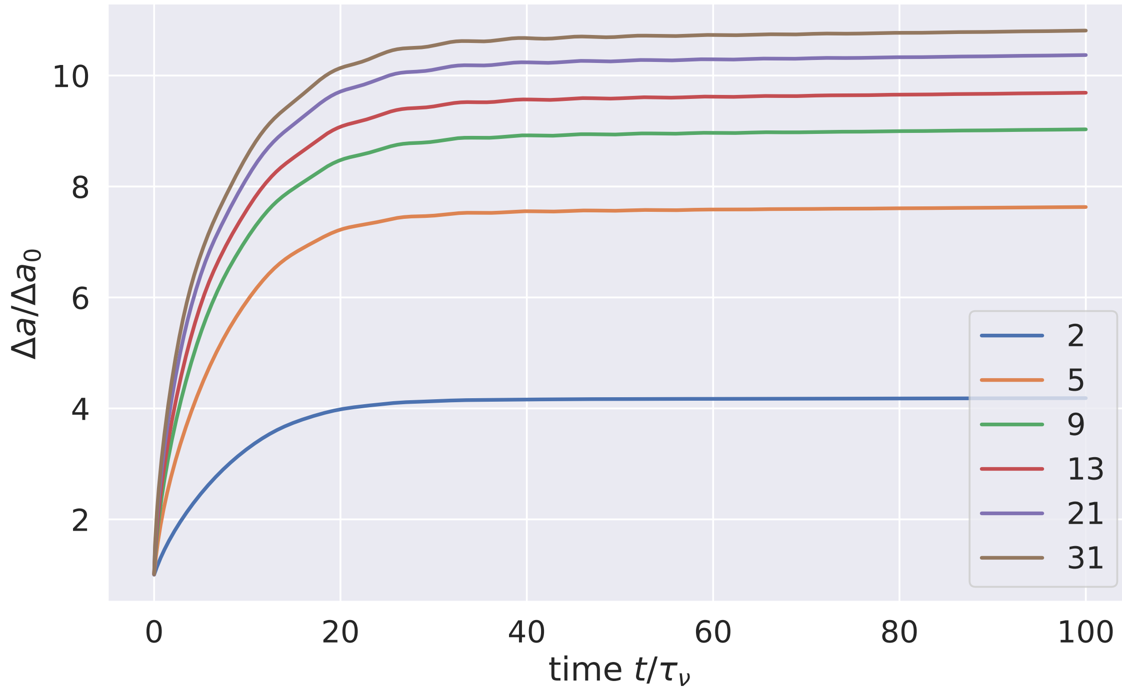

Figure 23. The nominal ringlet simulation is repeated for ringlets composed of $N_s = 2, 5, 9, 13, 21, 31$ streamlines as indicated by the legend, with all other parameters are identical to that used in Fig. 1. Plot shows how the simulated ringlets' semimajor axis width $\Delta a = a_{outer} - a_{inner}$ evolve over time t in units of the nominal ringlet's viscous timescale τ_ν.

widths $\Delta a = a_{outer} - a_{inner}$. Figure 24 plots each streamlines' final eccentricities e versus their final Δa, and this plot shows that all curves have the same e versus Δa slope *i.e.* all simulated ringlets have the same eccentricity gradient regardless of number of streamlines N_s. Ditto for $\tilde{\omega}$ versus Δa, Fig. 25. Consequently, the evolution of the simulated ringlets nonlinearity parameter q, which depends on those gradients via Eqn. (9), and also controls how viscosity communicate angular momentum between the streamlines [e.g. Eqn. (16) and note that $q \simeq e'$ in all simulations considered here], is very similar over time for various N_s, see Fig. 26. The only noteworthy difference between the $N_s = 2$ ringlet and the higher N_s ringlets is seen in Fig. 25, which which shows that the $N_s > 2$ ringlets have an outer longitude of peripase that trails the inner streamline by a factor of ~ 2. Except for this one distinction, the evolution of the $N_s > 2$ ringlets is very similar to that exhibited by nominal ringlet composed of $N_s = 2$ streamlines

4.7.1. *partially confined ringlets*

text...

5. RINGLET ORIGIN SCENARIOS

text...

6. SUMMARY OF FINDINGS

Main findings:

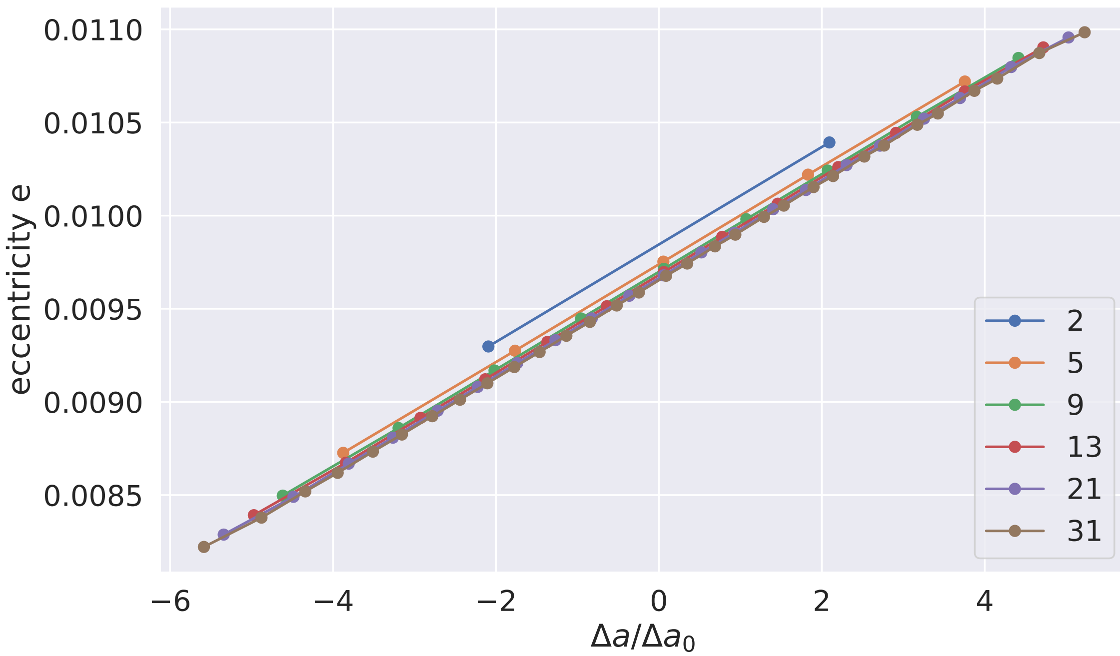

Figure 24. Simulated ringlets' final eccentricities e are plotted versus their final semimajor axis displacement $\Delta a = a - \bar{a}$ where $\bar{a}$ is the mean semimajor axis of all particles in each ringlet.

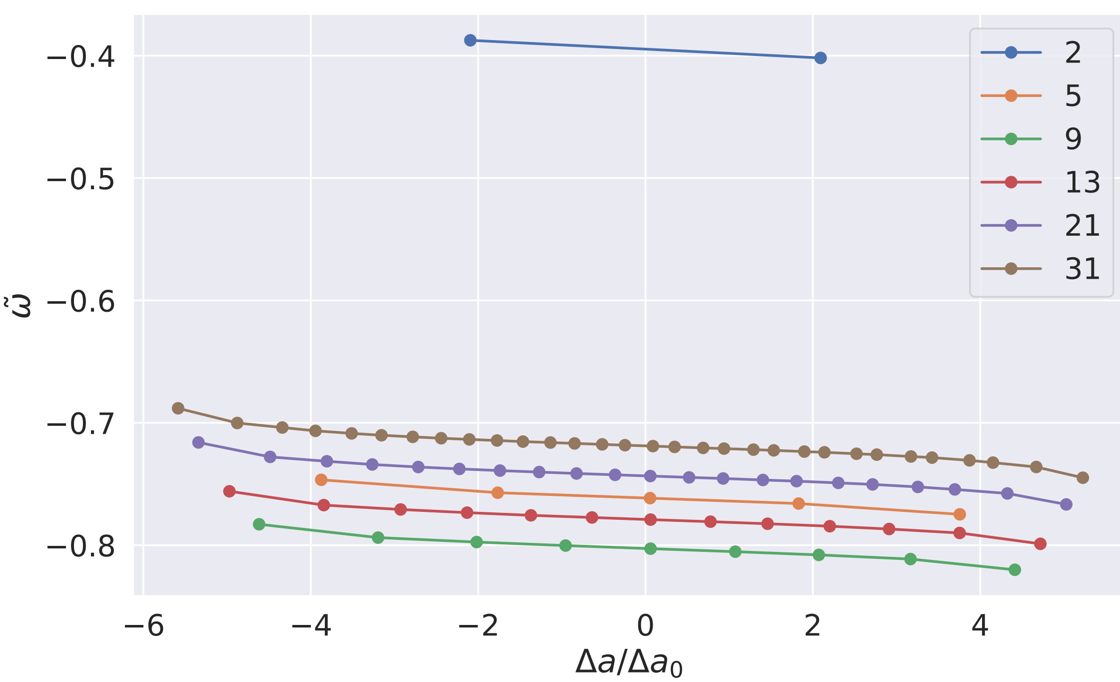

Figure 25. $\tilde{\omega} = \tilde{\omega}_{outer} - \tilde{\omega}_{inner}$

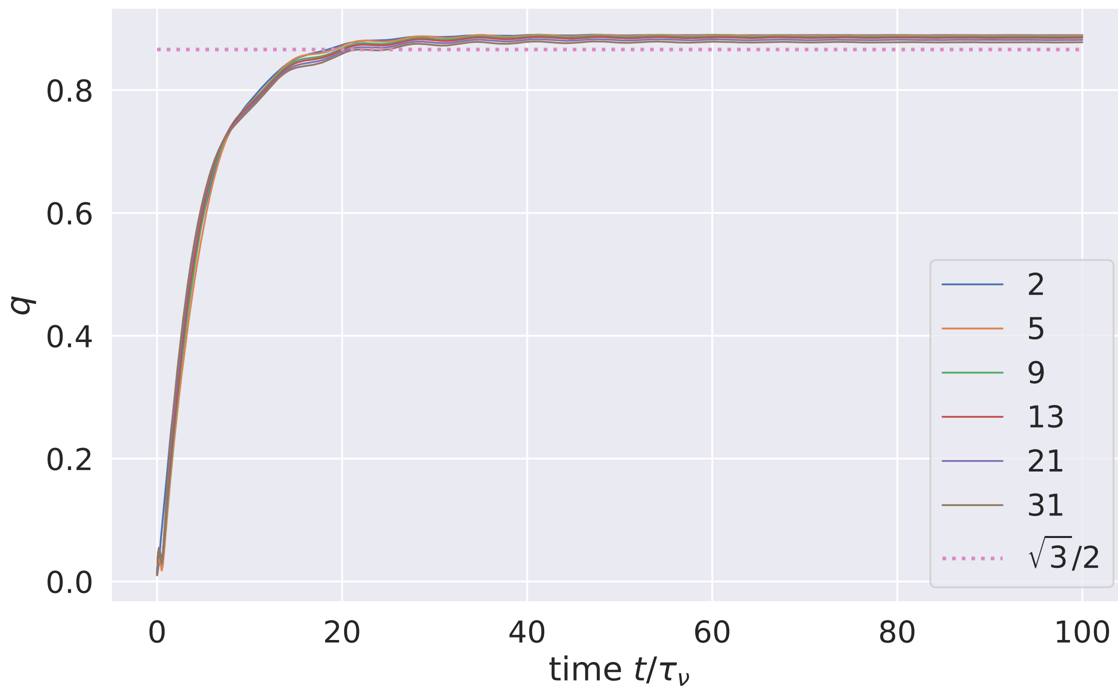

Figure 26. Caption...

1. Simulations show that narrow eccentric ringlets having a wide variety of initial physical properties (mass, initial width, viscosity) do evolve into the self-confining state (see Fig. 16), provided that the ringlet's initial eccentricity is sufficiently high (Section 4.5.3). Self-gravity causes the ringlet's eccentricity gradient e' to grow over time until they near the $\simeq e' \simeq \sqrt{3}/2 \simeq 0.866$ threshold where viscous angular momentum flux reversal is nearly complete and there is *almost* no radial orbit-averaged transmission of angular momentum due to the ringlet's viscous friction.

   Simulations also show that these self-confining ringlets all have a small periapse twist $|w'| \ll e'$ so that the ringlet's nonlinearity parameter is dominated by their eccentricity gradient $q = \sqrt{e'^2 + \tilde{\omega}'^2} \simeq e'$.

2. Self confining ringlets have $L_E = 0$

3. partial self confinement

7. FOLLOWUP STUDIES

Possible followup studies...

8. ACKNOWLEDGMENTS

This research was supported by the National Science Foundation via Grant No. AST-1313013.

APPENDIX

A. APPENDIX A

Derive the more accurate drift step used by epi_int_lite...

Show that angular velocity $\omega = v_\theta/r \simeq \Omega(1 + 2e\cos M)$ to first order in e. Then show that

$$\omega' = \frac{d\omega}{dr} \simeq -\left(\frac{3\Omega}{2a}\right)\frac{1-\frac{4}{3}e'\cos M}{1-e'\cos M} \tag{A1}$$

to lowest order in e where mean anomaly $M \simeq \theta - \tilde{\omega}$.

B. APPENDIX B

Compare epi_int_lite to theoretical predictions

C. APPENDIX D

This examines the viscous evolution of a narrow eccentric non-gravitating ringlet that is identical to the nominal ringlet of Section 3.1 but with ringlet self-gravity neglected and $J_2 = 0$. As the orange curve in Fig. 27 shows, the non-gravitating ringlet's radial width Δa grows steadily over time due to ringlet viscosity, long after the nominal self-gravitating ringlet (blue curve) has settled into the self-confining state by time $t \sim 15\tau_\nu$. This is due to the ringlet's secular gravitational perturbations of itself, which tends to excites the ringlet's outer streamline's eccentricity at the expense of the inner streamline (see Fig. 3) until the ringlet eccentricity gradient e' (blue curve in Fig. 28) grows beyond the limit required for complete angular momentum flux reversal that results in the ringlet's radial confinement (dotted line). Note that viscosity also excites the non-gravitating ringlet's eccentricity gradient some (orange curve), but not sufficiently to halt the ringlet's viscous spreading.

D. APPENDIX E

This Appendix will use the orbit elements derived in Appendix A to derive Eqn. 15 from 3, and then Eqn. (16).

E. APPENDIX F

Viscous and gravitational energy transport...

REFERENCES

Borderies, N., Goldreich, P., & Tremaine, S. 1982, Nature, 299, 209
—. 1983, Icarus, 55, 124
—. 1985, Icarus, 63, 406
Brouwer, D., & Clemence, G. M. 1961, Methods of celestial mechanics (New York: Academic Press, 1961)
Chambers, J. E. 1999, MNRAS, 304, 793
Chiang, E. I., & Goldreich, P. 2000, ApJ, 540, 1084
Goldreich, P., & Tremaine, S. 1979a, AJ, 84, 1638
—. 1979b, Nature, 277, 97
—. 1981, ApJ, 243, 1062
Hahn, J. M., & Spitale, J. N. 2013, ApJ, 772, 122
Longaretti, P. Y. 2018, Theory of Narrow Rings and Sharp Edges, ed. M. S. Tiscareno & C. D. Murray, 225–275
Mosqueira, I., & Estrada, P. R. 2002, Icarus, 158, 545
Pringle, J. E. 1981, ARA&A, 19, 137
Rimlinger, T., Hamilton, D., & Hahn, J. M. 2016, in AAS/Division of Dynamical Astronomy Meeting, Vol. 47, AAS/Division of Dynamical Astronomy Meeting, #47, id.400.02

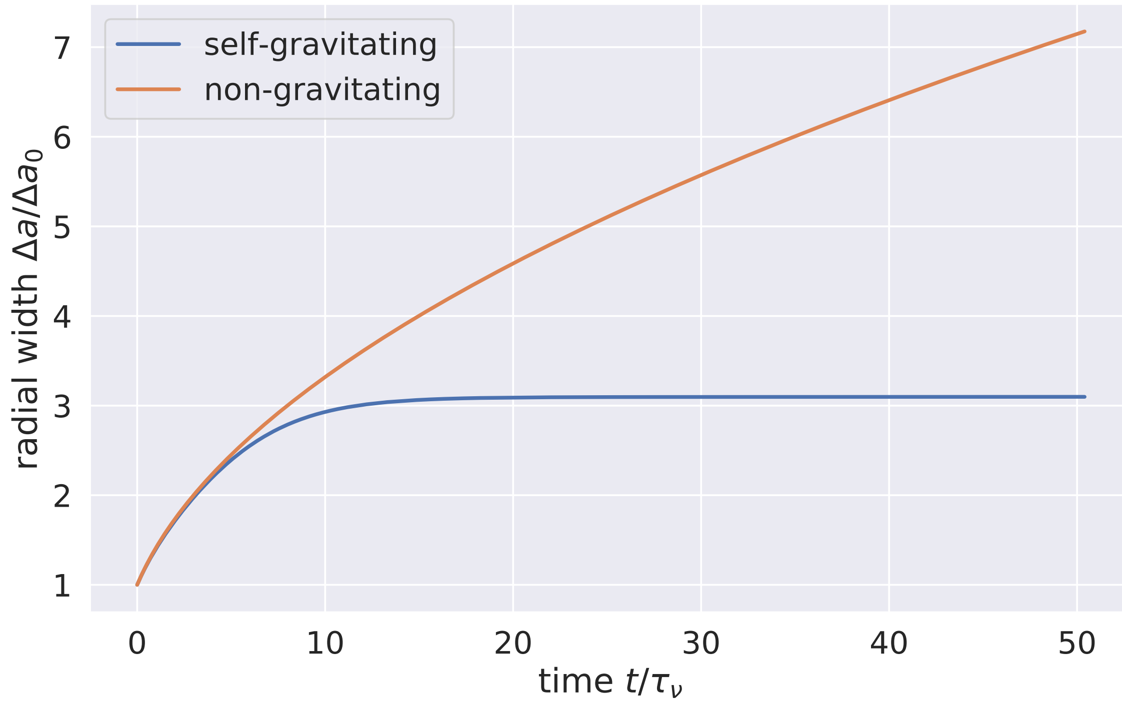

Figure 27. Blue curve is the nominal ringlet's semimajor axis width Δa versus time t, and this ringlet's radial spreading ceases by time $t \sim 15\tau_\nu$ when it's self-gravity has excited the ringlet's eccentricity gradient e' sufficiently; see blue curve in Fig. 28. Orange curve shows that the non-gravitating ringlet's Δa grows without limit due to the ringlet's much lower eccentricity gradient. Note that planetary oblateness would cause the non-gravitating streamlines to precess differentially and eventually cross when $J_s > 0$, so the non-gravitating simulation also sets $J_2 = 0$ to avoid differential precession.

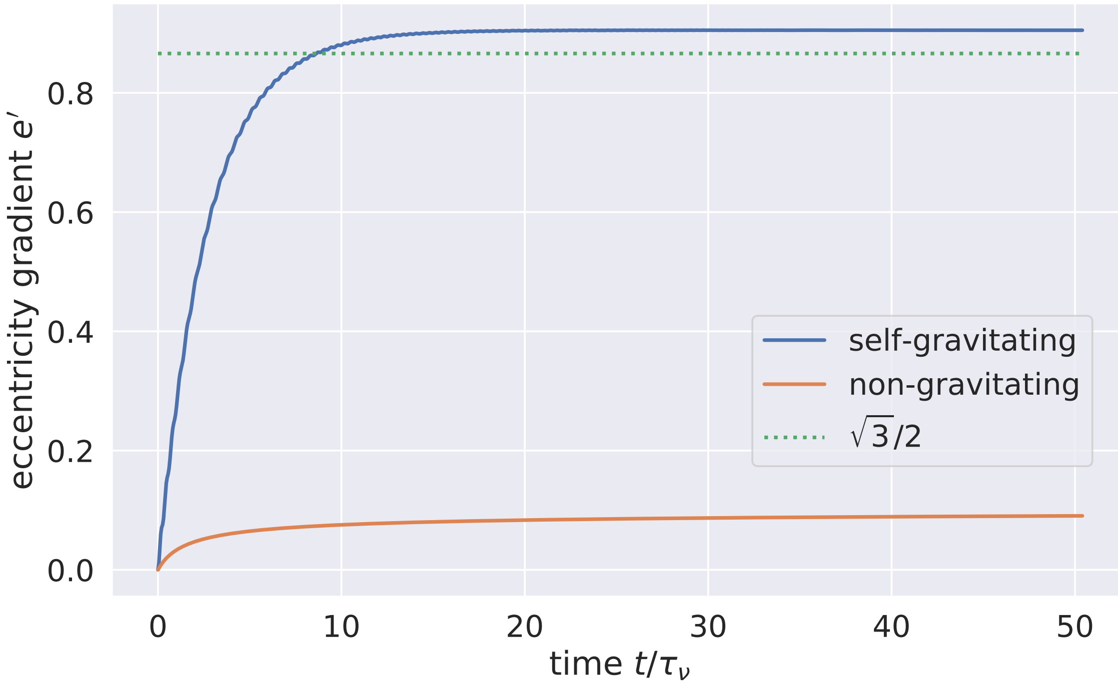

Figure 28. blah